ENGINEERED LINEAR AND NONLINEAR OPTICAL

PROPERTIES OF METAL-DIELECTRIC THIN-FILM

STRUCTURES FOR ULTRAFAST OPTICAL APPLICATIONS

A Dissertation
Presented to
The Academic Faculty

by

James June Fan Hsu

In Partial Fulfillment
Of the Requirements for the Degree
Doctor of Philosophy in the
School of Electrical and Computer Engineering

Georgia Institute of Technology
December 2013

ENGINEERED LINEAR AND NONLINEAR OPTICAL

PROPERTIES OF METAL-DIELECTRIC THIN-FILM

STRUCTURES FOR ULTRAFAST OPTICAL APPLICATIONS

Approved by:

Dr. Bernard Kippelen, Advisor
School of Electrical and Computer
Engineering
Georgia Institute of Technology

Dr. John A. Buck
School of Electrical and Computer
Engineering
Georgia Institute of Technology

Dr. Ian F. Akyildiz
School of Electrical and Computer
Engineering
Georgia Institute of Technology

Dr. Benjamin Klein
School of Electrical and Computer
Engineering
Georgia Institute of Technology

Dr. Joseph W.Perry
School of Chemistry and Biochemistry
Georgia Institute of Technology

Date Approved: October 25, 2013

ACKNOWLEDGEMENTS

The author would first like to thank his girlfriend Yan-Ling Chen, who encourages me to live up to crazy ideals, and strive to make this work possible. I sincerely thank the thorough support from my family for needs in all aspects and keep believing me.

This work could never be realized without helps from many people around me and our research lab. My advisor, Prof. Bernard Kippelen, guides my research direction and inspires me to develop potential applications out of a fundamental research in science. Our research scientist, Dr. Canek Fuentes-Hernandez, always mentors me to grow and refines our ideals through countless difficulties in research and life. He teaches me how to dream and how to chase a dream as a mentor and as a friend. I wish to thank our group members to create a great work environment, where I am proud to be one of them. My sincere appreciation also goes to Harold Solomon (venture lab, Georgia Tech), for seeking the commercialization opportunities on our inventions, and opening my eyes in the business vision.

I am grateful to Dr, Joel M. Hales and Dr. Josepph W. Perry for the fair amount of pulsed laser time and facilities I borrowed, and particularly thank Joel, who generously teaches me experimental skills and knowledge I lacked.

Thank you to all my committee for taking the time to approve this work.

TABLE OF CONTENTS

LIST OF TABLES

LIST OF FIGURES

LIST OF SYMBOLS AND ABBREVIATIONS

NLO   Nonlinear Optical

ITF   Induced Transmission Filter

SPPs   Surface Plasmon Polaritons

UV   Ultraviolet

WLC   White Light Continuum

Broadband NLO Device

The nonlinear optical device discussed in Section 3.1

Narrowband NLO Device

The nonlinear optical device discussed in Section 3.2

Ultrafast All-Optical Shutter

The ultrafast all-optical shutter discussed in Chapter 4

SUMMARY

The objective of the present dissertation is to advance the science and engineering of metal-dielectric thin-film structures for ultrafast all-optical applications. The research presented consists of three parts: first, the linear and nonlinear optical (NLO) properties of Au and Ag/Au bilayer metallic thin films are comprehensively studied; then the design and properties of a novel nonlinear device structure are presented and finally an ultrafast all-optical shutter is develop and applications are discussed. In the first part, this study describes the linear and NLO properties of bilayer metallic films and shows that they can be tuned by controlling the mass-thickness ratio between Au and Ag. The combined properties of these bilayers are attractive for active plasmonic applications and nonlinear optical filters. Detailed physical models describing the linear and NLO response of Au and Ag/Au bilayers are presented and compared with experiments. In the second part, these models are used to optimize the NLO response of a novel Au-based NLO device. With only four layers, this novel device strongly amplifies the NLO response of the component Au thin film. NLO devices with broad spectral and angular bandwidths in the visible spectral region are demonstrated. The narrow band dependent NLO response of the NLO device is shown to lead to all-optical controls of high peak-power optical signal pulses. Finally, the NLO device technology is integrated into a novel ultrafast all-optical shutter, which allows temporal sampling windows as short as a few ps. Ultrafast all-optical shutter potentially can temporally shape high peak-power nanosecond optical pulses, which could benefit biomedical and micromachining applications. Other possible optical applications such as short electron, X-ray pulse generations, ultrafast photography, and biomedical imaging will also be discussed.

CHAPTER 1: INTRODUCTION

1.1 Overview

The objective of the present dissertation is to advance the science and engineering of metal-dielectric thin-film structures for ultrafast all-optical applications. One of the main challenges to develop all-optical control applications in the visible spectral region has been the lack of NLO materials with strong NLO response at visible wavelengths. The state-of-the-art of NLO materials and devices in the visible spectral range will be described in CHAPTER 1. Through the research described in this dissertation novel metal-dielectric thin-film structures that amplify the strong and ultrafast NLO response of noble metal thin films are developed and used to demonstrate a novel ultrafast all-optical shutter technology in the visible spectral range. In CHAPTER 2, the linear and NLO properties of Au and Ag/Au bilayer metallic thin films are comprehensively studied with physical models and compared with experiments. In CHAPTER 3, a novel noble-metal NLO device structure is described and shown to lead to extremely large and ultrafast reflectance changes upon being excited by femtosecond optical pulses. The angular and spectral bandwidth of NLO devices are studied using two different designs: a broadband NLO device and narrowband NLO device. In CHAPTER 4, the NLO device technology is used to develop a novel ultrafast all-optical shutter capable of offering the ability to easily adjust the opening window (i.e. actively control the time during which the shutter remains open) in the ps to ns temporal regimes. Finally, the conclusion and future work is presented in CHAPTER 5.

1.2 Background of noble metals

Noble metals, such as Ag, Au, and Cu, have a wide range of applications in photonics and electro-optics. Within the visible and near-infrared spectral regions, Ag, Au, and Cu can have a negative permittivity that allows for the excitation of surface plasmon

polaritons (SPPs), which have been actively exploited in recent years for sub-wavelength photonic circuits [1]. This negative permittivity also enables artificial meta-material structures which allow remarkable control over the dispersion and sign of the refractive index of a material and consequently over the flow of electromagnetic energy throughout its structure [2]. In addition, highly transparent metallic structures [3] have been reported and are attractive as optical filters with high out-of-band rejection [4] and thin-film metal electrodes in organic light-emitting diodes [5]. Noble metals have also attracted great attention because their extremely large and ultrafast non-linear optical (NLO) response [6, 7] can be exploited to achieve all-optical control of metallic nanostructures [8-11]. This NLO response is described as the first-order nonlinear susceptibility $\chi^{(1)}$ process caused by electron and lattice heating [6, 7, 12].

In the early studies, optical nonlinearities of noble metals have been interpreted in the context of the third-order nonlinear susceptibility $\chi^{(3)}$ process measured by standard techniques such as Z-scan and degenerate four-wave mixing (DFWM) for the characterization of the NLO properties [13]. The magnitude of $\chi^{(3)}$ have been estimated at visible wavelengths on the order of 10^{-9}-10^{-8} esu (10^{-17}-10^{-16} m^2/V^2) for Ag [14, 15], 10^{-8}-10^{-7} esu (10^{-16}-10^{-15} m^2/V^2) for Au [15, 16], and 10^{-7}-10^{-6} esu (10^{-15}-10^{-14} m^2/V^2) for Cu [17]. Most of these estimations arise from measurements performed in nanocermets (metal-nanoparticles embedded in a dielectric host) and rely in the use of some effective medium theories to extract the intrinsic response of the metallic component. The third-order nonlinearity is an intensity-dependent nonlinear effect so-called optical Kerr effect, wherein the value of $\chi^{(3)}$ coefficient is an intensity-independent constant, and the nonlinear response is instantaneous on the sub-femtosecond time scale.

However, the instantaneous Kerr effect was found inadequate to describe the NLO properties of noble metals through experimental studies. First, the $\chi^{(3)}$ coefficients of noble metal thin films measured from Z-scan techniques, are not intensity-independent constants and their values could vary significantly by two order-of-magnitudes with

different pulse intensities and pulse widths [6]. Second, the nonlinear responses of noble metal thin films [18, 19] and nanoparticles [20, 21] have revealed a non-instantaneous temporal evolution studied by pump-probe experiments. In addition, thermo-modulations experiments have also been conducted to provide extensive evidence, in which the thermal dynamics of electrons can modify the permittivity of metals [22-24]. In fact, until the electron heating is recognized as the strongest contribution to the NLO response of metals, the dynamic of their nonlinearities is eventually interpreted accurately according to the two-temperature model [25, 26]. The two-temperature model describes the ultrafast heating process of electron and lattice temperatures and will later be presented in details in this dissertation.

It is interested to note that after the role of ultrafast thermal effects was discovered in noble metals, Conforti et $al.$ have derived a non-instantaneous $\chi^{(3)}$ coefficient of an Au film, assuming continuous-wave pump and probe, with a pump wavelength $\lambda_a = 950$ nm (frequency ω_a), and a probe pulse wavelength $\lambda_b = 500$ nm (frequency ω_a), they estimate values of $\chi^{(3)}$ (ω_b; ω_a, -ω_a, ω_b) $\approx$ (-8.4 + 11i) $\times$ 10^{-8} esu ((-1.2 + 1.5i) $\times$ 10^{-15} m^2/V^2), about six orders of magnitude larger than fused silica [27]. This non-instantaneous $\chi^{(3)}$ coefficient is still derived from the two-temperature model, but offers an extended version to interpret ultrafast thermal nonlinearities of noble metals. It is important to note that non-instantaneous $\chi^{(3)}$ coefficients of noble metals are pulse width dependent and intensity dependent as shown by Rotenberg $et.al$ and implicit in the derivation of Conforti $et.al$. For instance, the imaginary part of $\chi^{(3)}$ is sometimes discussed in form of nonlinear absorption coefficient β to describe the nonlinear absorption process, and the effective value of β_{eff} was reported to change by nearly two orders of magnitude from 6.8×10^{-7} to 6.7×10^{-5} cm/W as the pulse width varied from 0.1 to 5.8 ps, measured for 20-nm thick Au at 630 nm [6].

Although a direct comparison is difficult to make between non-instantaneous $\chi^{(3)}$ coefficients of noble metals and instantaneous $\chi^{(3)}$ coefficients of other NLO materials,

3

$\chi^{(3)}$ coefficient values are listed below as a general reference on magnitudes. Most NLO materials display values of $\chi^{(3)}$ that are orders-of-magnitude smaller than those estimated for noble metals, for example, glasses such as fused silica or BK-7 glass at 1.91 μm displays a value of 10^{-14} esu (10^{-22} m^2/V^2) [28, 29]; semiconductors such as ZnSe or GaAs at 1.06 μm display values of 10^{-12}-10^{-10} esu (10^{-20}-10^{-18} m^2/V^2) [28]; polymers such as 4BCMU (4-butoxycarbonylmethyl-urethane-polydiacetylene) at 1.06 μm or bisdioxaborine polymethines at 1.3 μm display values of 10^{-11}-10^{-10} esu (10^{-19}-10^{-18} m^2/V^2) [28, 30, 31]. Note that these materials with large instantaneous $\chi^{(3)}$ coefficients are located at the infrared spectral range instead of the visible spectral range.

The larger order of magnitude in the non-instantaneous $\chi^{(3)}$ values derived by Conforti *et al* can only be compared with the following instantaneous $\chi^{(3)}$ values: nanoparticles such as CS-doped glass (Commercial glass, Corning #3484: CS3-68) at 532 nm or Au-doped glass at 550 nm displays values of 10^{-9}-10^{-7} esu (10^{-17}-10^{-15} m^2/V^2) [28, 32, 33]; Polymers such as PTS (p-toluene sulfonate) at 1.06 μm displays values of 10^{-8} esu (10^{-16} m^2/V^2) [28, 34].

The linear and nonlinear optical responses of a noble metal and their potential applications are determined by the inherent electronic response which gives rise to their dielectric permittivity. The electronic response of a noble metal in the visible spectral region can be divided into two separate mechanisms: interband and intraband electronic transitions [26, 35]. Electronic interband transitions in the visible or ultraviolet (UV) spectral region arise from bound electrons excited from fully occupied electronic states within the d-band, below the Fermi energy level, to the half-filled s-p electronic bands in the conduction band. In this spectral region, metals are opaque because optical fields are strongly absorbed. At lower energies, electronic intraband transitions occur from free electrons stimulated within the conduction band. In this spectral region, metals are opaque mainly because the optical fields are reflected off its surface, rather than absorbed in the bulk.

When a metal is excited with an ultrafast optical pulse, the energy absorbed by the electron gas raises its temperature and smears the electronic distribution around the Fermi energy (Fermi-smearing), causing a very strong change of the dielectric permittivity of the metal around the onset of interband region [26]. In the intraband region, an increased electron temperature increases electron scattering processes which change the dielectric permittivity, albeit these changes are of smaller magnitude than the ones produced in the onset of the interband region [7]. Therefore, noble metals such as Au and Ag have very different linear and nonlinear optical properties not only because of inherent differences in their electronic configurations, but also because these differences cause the onset of interband transitions to lie in very different spectral regions (in the visible for Au and in the UV for Ag).

Noble metals are known to have an extremely large and ultrafast NLO response in the visible spectral range, much larger than most known organic or inorganic materials, but are seldom used as NLO materials due to their limited optical transparency and large reflectance in the visible and near-infrared spectral ranges. Ultra-thin layers of noble metals can be semi-transparent in the visible range if their thickness is around the skin depth of metals (typically between 10 to 20 nm). Thicker metal layers rapidly loose transparency and become highly reflective due to the inherent large admittance contrast between metals and the dielectric environment. It is well known in the art that the dielectric environment of a metal can be engineered, by nanostructured dielectric layers, to relief the admittance contrast between the metal and its environment. Using this approach, it is possible for thin layers of noble metals, with a thickness of several times its skin depth, to be highly transparent within the spectral region where the optical response of the metal arises from their intraband electronic transitions. The large admittance mismatch, or alternatively permittivity contrast, between metals and dielectrics makes it possible to engineer compact nanostructures with fewer layers and unique optical properties compared to all-dielectric nanostructures. Induced-transmission

filters (ITFs) [3] and metal-dielectric bandgap structures (MDPBGs) [36] are known examples of such nanostructures. The increased transmittance in such nanostructures arises from a large decrease in reflectance and an increased absorptance within the metal layers. Hence, metallic nanostructures offer a unique opportunity to engineer optical devices with tailored linear optical properties in the visible and NIR spectral ranges.

The ability to engineer the linear absorption in a thin metal layer within a nanostructure is important because the NLO response of noble metals arises from the electron and lattice heating [6] caused by the absorption of energy from an ultrafast optical pulse. Hence, engineering linear and NLO properties of metallic nanostructures opens the opportunity to develop a wide range of all-optical applications in the visible and near infrared spectral region where materials with ultrafast and strong NLO response are very scarce and where there is a need to develop a technology that could allow a new generation of all-optical devices

For all-optical applications in the visible spectrum, Au is an attractive material because its interband transition onset lies around 520 nm [37], causing a very large NLO response across the whole visible spectrum. The nonlinear optical changes of an Au thin film has been extracted from pump-probe experiments and shown to be strong, spectrally broad, and ultrafast [18]. In this dissertation, a novel Au based NLO device structure that allows all-optical control of its reflectance will be presented. The easily fabricated four-layer metal-dielectric thin-film structure will provide large and ultrafast reflectance changes in the visible spectral range. Its adjustable spectral and angular bandwidth will also be demonstrated in two structure designs: broadband NLO device and narrowband NLO device.

1.3 Origin and history of the problem

Materials with a strong power-dependent reflectance, transmittance, or absorptance are keys for the development of all-optical applications such as optical signal processing

[38], pulse compression [39], passive protective devices [40], and medical image processing [41, 42]. Different types of nonlinear optical (NLO) effects and materials have been used to realize NLO devices. Take nonlinear reflectors for example, the combination of a second harmonic generation (SHG) crystal and a dichroic mirror has been used to demonstrate intra-cavity passive mode-locking operation for picosecond-pulse generation in the visible range [43, 44]. In addition, Bragg-periodic structures comprising semiconductor layers with Kerr optical nonlinearity in the infrared spectral range have been reported [38, 45]. A common limitation of these approaches is that they require complex structures which have restrictive wave-vector matching conditions that are difficult to implement due to the need of precise optical alignment.

NLO devices have mostly been implemented in the near-infrared and infrared spectral ranges because NLO materials in the visible spectral region are scarce. The most commonly used NLO materials are semiconductors, but their prominent nonlinearities mainly locate at infrared or near infrared wavelengths [46]. All-optical applications in visible region have been limited by the lack of materials and devices with a strong NLO response. The rapid-growth development of biomedical applications and micromachining using ultrafast optical pulses in the visible spectral range creates a strong need for developing ultrafast optical devices that can operate at visible and near-infrared wavelengths. These devices can perform all-optical control over the spatial and temporal irradiance profiles of high energy optical pulses and could potentially be attractive for a multiple applications related to the use of ultrafast optical pulses.

Ultrafast laser pulses with nanosecond, picosecond, and femtosecond temporal pulse widths are used to drill, cut, or machine products for the microelectronics, biotechnology, photonics, precision engineering and medical industries. Pulsed lasers offer fast and cost-efficient prototyping of products made from any material, like ceramics, glasses, plastics, or metals, just to mention a few. Furthermore, pulsed lasers are now also used in a wide variety of surgical procedures [47] such as eye [48], dental

[49], blood-vessel [50], and endoscopic surgeries (i.e. removal of deep-sealed tumors or treating scarred vocal folds [51]). This is because high peak-power laser pulses are able to ablate materials with a high spatial precision in a fast and cost-effective way.

It is well established that the ability of a laser to ablate a material and the quality of the ablation depends upon the power and energy of the laser pulse and very importantly, on its temporal pulse width. High peak-power nanosecond lasers ablate materials by conventional heat deposition (heating of the lattice) that results in melting and vaporization of the material, and occasionally, in fracture. This process is known as thermal ablation of materials and results in a heat-affected zone surrounding the ablated spot. In contrast, high peak-power sub-nanosecond lasers with temporal pulse widths smaller than a few hundreds of picoseconds produce multi-photon ionization, joule heating, avalanche ionization, and plasma formation with a greatly reduced or non-existent heat-affected zone. For these reasons, nanosecond lasers are being replaced by sub-nanosecond pulsed lasers in surgical or manufacturing applications requiring high tolerances; this is, fine ablations with reduced or non-existent thermal side-effects.[52, 53].

The problem faced by non-thermally ablating materials is that high peak-power sub-nanosecond pulsed lasers are expensive to own, operate, and maintain. High capital investments and recurring costs currently limit the wide spread adoption of these technologies. Therefore, this dissertation will not only present the NLO devices developed from the understanding of linear and NLO properties of metal thin films, but also integrate the NLO device technologies into a novel ultrafast all-optical shutter. This ultrafast all-optical shutter is proposed to allow sampling of high peak-power nanosecond laser pulses to produce high peak-power picosecond or femtosecond pulses that are well suited for non-thermal ablation of materials. Although the experimental work of the ultrafast all-optical optical shutter is still at the early proof-of-principle stage, it has a potential to replace expensive high peak-power sub-nanosecond lasers with less

expensive nanosecond lasers; thereby, significantly decreasing the capital equipment and recurring cost for high-quality pulsed laser manufacturing and laser surgery.

The commercialization potential of the ultrafast all-optical shutter was investigated through a Nation Science Foundation funded program (NSF-iCORPS). An extensive study has been conducted by interviewing people in a wide variety of companies such as laser contracting service, laser integration, laser tattoo removal, laser engravers, pulsed laser deposition (PLD), and research institutes conducting ultrafast spectroscopic and imaging studies. It was found that if applied to slice ultrafast laser pulses, the ultrafast all-optical optical shutter technology will need further developments and demonstration of outstanding cutting resolutions and speeds to compete with existing advanced sub-nanosecond pulsed laser. It was also found that other possible optical applications might offer more attractive avenues for development and potential commercialization of the ultrafast all-optical shutter technology, such as short electron beam and X-ray pulse generations, ultrafast photography, and biomedical imaging.

CHAPTER 2: LINEAR AND NONLINEAR OPTICAL PROPERTIES OF Au AND Ag/Au BILAYER THIN FILMS

Ag, Au, and configurations of Ag/Au bilayer thin films have also been used to solve multiple engineering problems. For instance, high chemical stability and high sensor sensitivity have been achieved by using Ag/Au bilayer films in different surface plasmon resonance (SPR) sensor designs [54, 55]. Al/Ag bilayer films have also been used as transparent electrodes in top-emitting organic light-emitting diodes [56]. Additionally, the interactions between multi-layer metal films and femtosecond laser pulses have been studied in terms of increasing the damage threshold of laser mirrors [57, 58]. However, little attention has been directed at understanding the linear and nonlinear optical properties of Ag/Au bilayer thin films by controlling the thickness ratio between the two metals.

The linear and nonlinear optical properties of Au and Ag/Au bilayer metallic thin films with a total thickness of around 20 nm and with different Ag/Au mass-thickness ratios are present. This study shows that the spectral dispersion of the effective refractive index of bilayer films preserves the general dispersion features found in their component materials, namely distinct interband-like and intraband-like transition regions. In addition, it is also shown that the effective refractive index can be tuned spectrally by controlling the mass-thickness ratio between gold and silver. As a consequence, it is shown that the magnitude and spectral dispersion for the NLO response of the bilayer films can also be tuned. These changes are modeled using the two-temperature model and a physical model that describes the dielectric permittivity in terms of their interband and intraband transition terms. Potential linear and nonlinear optical applications of these metallic bilayers are also discussed.

2.1 Fabrication and characterization

Three thickness ratios of Au and Ag with a total thickness of 20 nm bilayer Ag/Au films were fabricated. Single layers of Au and Ag were fabricated as reference samples with the same total thickness. Single layer and bilayer metallic samples with the following geometry were deposited:

R1: Glass/ Au (23 nm),
S1: Glass/ SiO$_2$ (64 nm)/ *M1*/ SiO$_2$ (98 nm),
S2: Glass/ SiO$_2$ (64 nm)/ *M2*/ SiO$_2$ (98 nm),
S3: Glass/ SiO$_2$ (64 nm)/ *M3*/ SiO$_2$ (98 nm),
R2: Glass/ Ag (20 nm),

where Au (23 nm) and Ag (20 nm) corresponds to a 23 nm and 20 nm thick Au and Ag film, respectively, and *M1* corresponds to Ag (4 nm)/Au (14 nm), *M2* to Ag (10 nm)/ Au (10 nm), and *M3* to Ag (15 nm)/ Au (6 nm) bilayers. The layer thicknesses (shown inside the parentheses) were individually estimated by matching transfer matrix method simulations with measured values of the transmittance (*T*), reflectance (*R*), and absorptance (*A*) spectra taken by a Shimadzu UV-Vis-NIR scanning spectrophotometer. Refractive index values of deposited Au (23 nm) and Ag (20 nm) films were obtained by modeling spectroscopic ellipsometric (SE) data (J.A. Woollam M-2000UI), taken on individual films, as a perfectly flat continuous layer. The effective refractive indices (N_{eff} = $n_{eff} + ik_{eff}$) of the bilayer films were calculated from SE data imposing Kramers-Kronig consistency to the calculated values.

The nonlinear optical properties (NLO) of these films were characterized by a commercially available white-light continuum (WLC) pump-probe spectroscopy system (Helios, ultrafast system). The pump pulse obtained from an optical parametric amplifier (TOPAS-C, Spectra-Physics) was tuned to a wavelength of 560 nm. A laser beam from a Ti:Sapphire regenerative amplifier (Spitfire, Spectra-Physics) operating at 800 nm pumped the TOPAS-C, while a small portion of this beam generated the WLC (420 - 950 nm) probe pulse. The WLC probe pulse measured 60 μm half-width-1/e (HW 1/e) at the

sample position using a knife-edge scan, and the pump pulse was 285 μm (HW 1/e). Because the probe size is significantly smaller than the pump, it is assumed that the probe overlaps with a region of approximately constant peak fluence from the pump. The pump has a pulse width of 60 fs (HW 1/e) and the total instrument response time is 150 fs full-width-half-maximum (FWHM). The pump beam was chopped at 500 Hz with a 50% duty cycle to obtain pumped (signal) and non-pumped (reference) probe spectra sequentially.

After averaging over one thousand probe pulses at each time delay, the change in optical density ($\Delta OD(\lambda, t)$) was recorded as a function of wavelength (λ) and delay time (t). The fluence of the probe pulses for all samples was confirmed to be low enough to produce no observable NLO response. Scattered pump light was subtracted from the data based on measurements at negative delay times. A temporal correction factor was applied to all data sets to provide equivalent zero delay onsets for all probe wavelengths; this correction factor was determined by measuring the chirp of the WLC probe passing through the glass substrate. The transmittance spectra change ($\Delta T(\lambda, t)$) and reflectance spectra change ($\Delta R(\lambda, t)$) of the WLC probe pulses were calculated from measured $\Delta OD(\lambda, t)$ as a function of delay time for a variety of pump fluences by

$\Delta T(\lambda, t) = -\ln(10) T(\Delta OD(\lambda, t))$ and $\Delta R(\lambda, t) = -\ln(10) R(\Delta OD(\lambda, t))$, where T and R are the linear transmittance and reflectance spectra, respectively. This formula is derived from a Taylor series expansion and therefore is only valid for small values of $\Delta OD(\lambda, t)$.

2.2 Linear optical properties
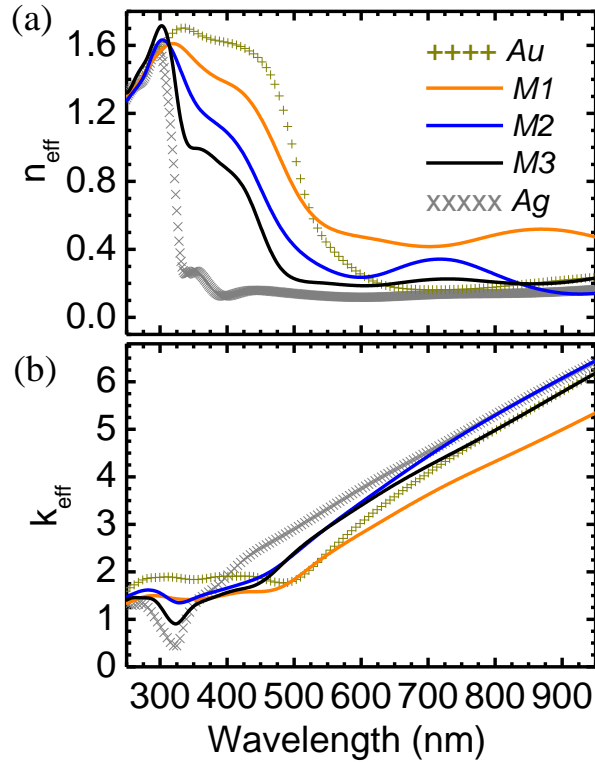
Figure 1: (a) real and (b) imaginary effective refractive index values of bilayer Ag/Au metal thin films: *M1*, *M2* and *M3*; Au (23 nm) and Ag (20 nm) are shown as reference.

Figure 1 (a) and 1(b) show the N_{eff} values of bilayers *M1*, *M2* and *M3*, as well as the refractive index values of single layer Au (23 nm) and Ag (20 nm). For Au (23 nm) and Ag (20 nm), the index values are close to literature values, with the interband transition onset of bulk Au [37] located at 520 nm and the interband transition onset of bulk Ag [26] at 313 nm. At these wavelengths, inflection points are present in the real part of refractive index. In contrast, for *M1*, *M2* and *M3* the inflection point in N_{eff} in the visible range moves away from Au (23 nm) and towards Ag (20 nm) as the thickness ratio of Au to Ag decreases, resulting in an apparent blue shift of the onset of interband transitions (Figure 1(a)). In other words, by controlling the Ag/Au mass thickness ratio in these

bilayers metallic films, the apparent onset of interband transitions can be spectrally tuned. This tunability, as will be described next, can be attractive for a variety of linear and nonlinear photonic applications.

Two figures-of-merit or quality factors have been recently introduced by Blaber, et al. [59] to evaluate the potential of metals for plasmonic applications. The first quality factor (Q_{LSP}) relates to the proficiency of a metal, with permittivity $\varepsilon = \varepsilon' + i\varepsilon''$, to sustain localized surface plasmon (LSP) excitations. Q_{LSP} is defined by the ratio - $\varepsilon' / \varepsilon''$, which can be directly related to, for instance, the resolving power of a single layer or multilayer superlens. The second quality factor (Q_{SPP}) relates to the proficiency of a metal to sustain surface plasmon polartions (SPPs). Q_{SPP} is defined by the ratio $(\varepsilon')^2 / \varepsilon''$, which is directly related to the propagation length of SPPs in plasmonic waveguides.
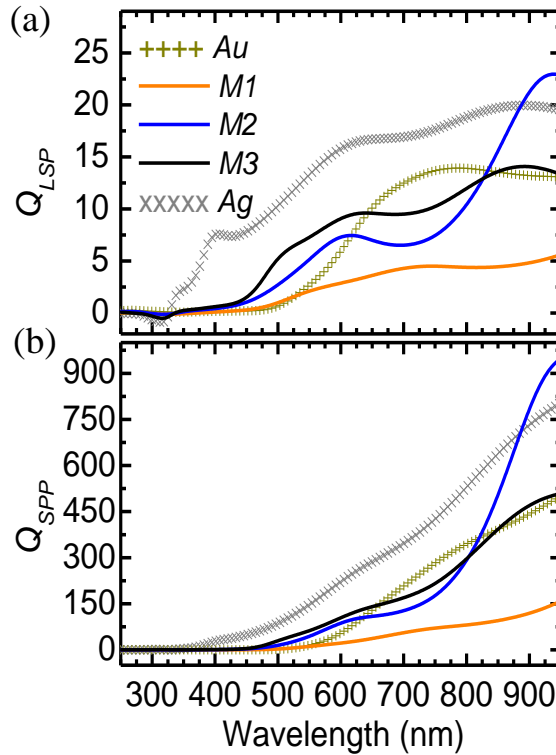
Figure 2: (a) Quality factor spectra for localized surface plasmon and (b) quality factor spectra for surface plasmon polariton of bilayer Ag/Au metal thin films: M1, M2 and M3; Au (23 nm) and Ag (20 nm) are shown as reference.

14

Figure 2(a) and 2(b) shows the spectral dispersion of Q_{LSP} and Q_{SPP} calculated for *M1*, *M2*, *M3*, Au (23 nm) and Ag (20 nm). The permittivity of each film was calculated from the $N_{eff} = \varepsilon^{1/2}$ values (Figure 1(a) and 1(b)). Note that Au (23 nm) always displays lower quality factors Q_{LSP} and Q_{SPP} values than Ag (20 nm). Strong absorptive losses in Ag (20 nm) due to interband transitions limit Q_{LSP} and Q_{SPP} values in the UV wavelength range from 250 to 350 nm. For Au (23 nm), the same mechanism also limits the values of Q_{LSP} and Q_{SPP} in the wavelength range from 250 to 500 nm. In this wavelength range, the apparent tuning of the onset of interband transitions achieved by decreasing the mass thickness ratio of Au to Ag leads to higher Q_{LSP} and Q_{SPP} values for all bilayer Ag/Au films compared to Au (23 nm). For instance, at wavelength 490 nm, Q_{LSP} improves from a value of 0.47 for Au (23 nm), to values of 0.79 for *M1*, 2.3 for *M2*, and 4.5 for *M3*. In contrast, at this wavelength $Q_{LSP} = 9.8$ for Ag (20 nm). Similarly, at 490 nm, Q_{SPP} improves from a value of 0.89 for Au (23 nm), to values of 1.9 for *M1*, 11 for *M2*, and 23 for *M3*, while for Ag (20 nm) it has a value of 78, although for wavelengths above ~600 nm, the quality factors for Au (23 nm) are higher than for any of the bilayers. It is interesting to note that in the range from 825 to 950 nm, *M2* shows Q_{LSP} and Q_{SPP} values that are again higher than Au (23 nm) and even higher than Ag (20 nm). Hence, although for linear plasmonic applications Ag (20 nm) displays higher quality factors in general, for applications that would require ultrafast all-optical plasmonic control [10], the bilayers will offer a very attractive combination of properties since the NLO response of any of the bilayers is significantly larger than that of *Ag*, as described in the next section. Finally, it should be noted that the values of N_{eff} and consequently Q_{LSP} and Q_{SPP} are dependent on the metallic film morphology, which is dependent on the conditions for the deposition of these metallic films. Hence, the results described here represent only general trends to be expected for a given deposition process.
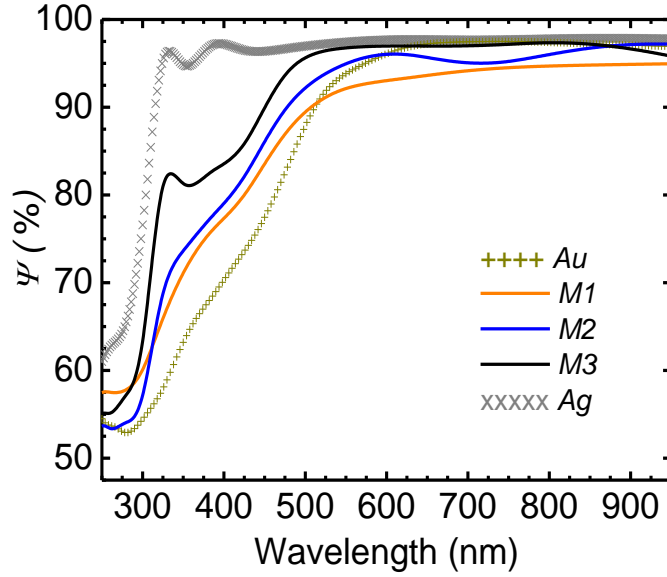
Figure 3: Simulated maximum potential transmittance spectra of bilayer Ag/Au metal thin films: M1, M2 and M3; Au (23 nm) and Ag (20 nm) are shown as reference.

For applications of Ag/Au bilayer films in linear optical filters, such as band pass filters (metal-dielectric band gap structures, induced transmission filters, etc.) or as transparent electrodes in electro-optic devices, the concept of maximum potential transmittance is useful since it provides an upper limit to the transmittance of an absorbing film, after all reflectance losses are suppressed. The maximum potential transmittance, Ψ, for a single metallic film was defined as a function of the layer thickness and the refractive index by Macleod *et al.* [60]. In Figure 3, the values of the maximum potential transmittance for Ag (20 nm), Au (23 nm), and bilayer films are compared by using the N_{eff} values previously derived and assuming films of equal thickness, 20 nm, to provide a fair comparison. Note that as a general statement, Au (23 nm) always displays lower values of Ψ than Ag (20 nm). For wavelengths 350- 500 nm, strong absorptive losses in Au (23 nm) due to interband transitions limits the values of Ψ compared to Ag (20 nm), which has an interband transition region in the UV range. As expected from the apparent tuning of the onset of interband transitions, decreasing the ratio of Au to Ag leads to larger values of Ψ in all Ag/Au bilayer films compared to Au

16

(23 nm), in the 350- 500 nm wavelength range. For instance, at wavelength 400 nm, Ψ improves from 70% for Au (23 nm) to 77% for *M1*, 79% for *M2*, and 84% for *M3*, as the thickness ratio of Au to Ag decreases as shown in Figure 3. In the 500- 950 nm range, bilayer films do not display improved values of Ψ but remain still higher than 90%. Once more, although Ag offers better linear optical properties across the visible spectrum, its more reactive nature to the environment and its much smaller NLO response make it less attractive for applications where improved environmental stability and higher NLO response are required.

2.3 Nonlinear optical properties

Potential applications for all-optical control that use the very large magnitude of the NLO response of noble metals, Au and Cu in particular, make it interesting to explore the NLO response of these bilayer films. The largest NLO response in a thin film of a noble metal arises due to the so-called Fermi smearing process. This process is driven by the rapid heating of electrons upon the absorption of energy from an ultrafast optical pulse. The rise of electronic temperature broadens the electronic distribution around the Fermi energy, at the onset of interband transitions, causing a drastic change of the permittivity of the metal [26].

2.3.1 Pump-probe experiments
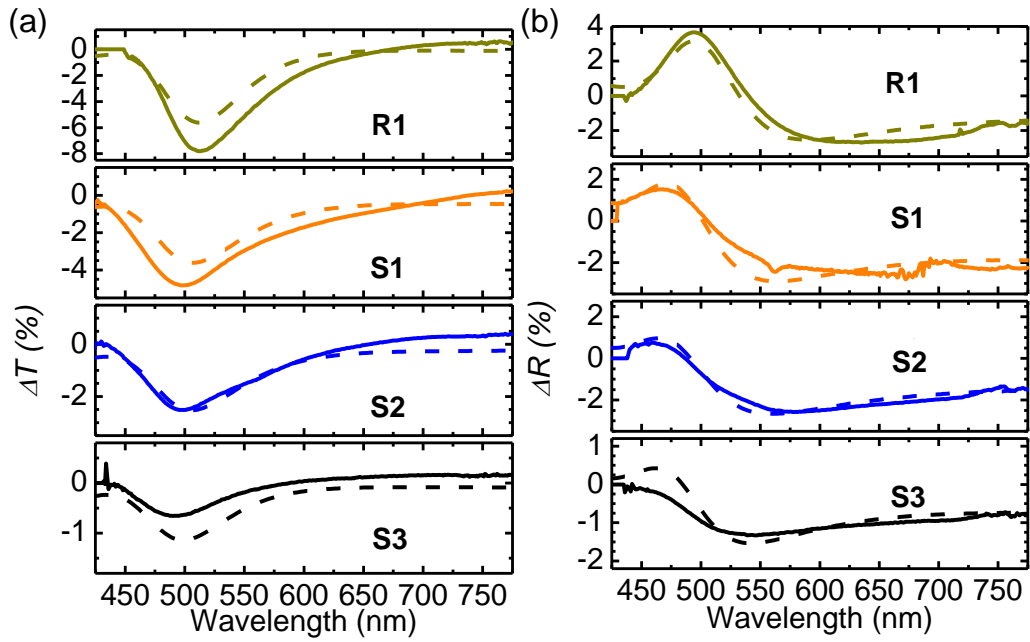
Figure 4: (a), (b) Spectral dependence of transmittance and reflectance changes ($\Delta T(\lambda, t_{peak})$ and $\Delta R(\lambda, t_{peak})$) measured from WLC pump-probe experiment (solid line) and simulation by two-temperature model (dashed line) of samples R1, S1, S2 and S3 with a pump fluence of 25 J/m^2. The excitation wavelength in all cases was 560 nm.
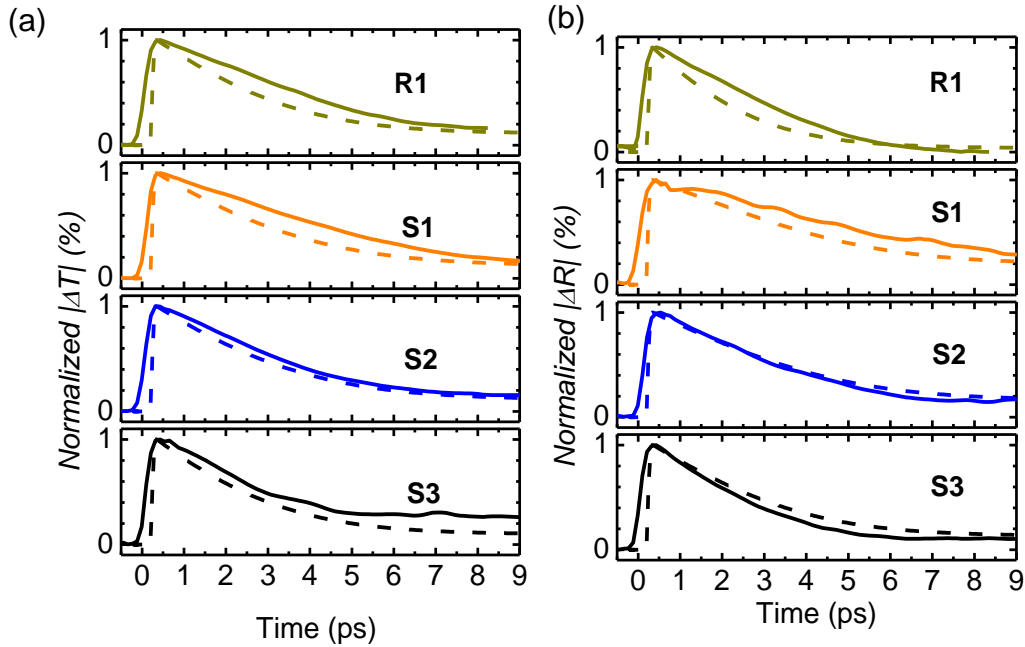
Figure 5: (a), (b) Temporal dependence of normalized absolute transmittance and reflectance changes ($|\Delta T(\lambda_{peak}= 520$ nm$, t)|$ and $|\Delta R(\lambda_{peak}= 520$ nm$, t)|$) measured from WLC pump-probe

experiment (solid line) and simulation by two-temperature model (dashed line) of samples R1, S1, S2 and S3 with a pump fluence of 25 J/m^2. The excitation (pump pulse) wavelength in all cases was 560 nm and the probe wavelength was 520 nm.

Figure 4(a) and 4(b) show the values of $\Delta T(\lambda, t_{peak})$ and $\Delta R(\lambda, t_{peak})$ measured in WLC pump-probe experiments in samples **R1**, **S1**, **S2**, and **S3** for a pump fluence of 25 J/m^2. Figure 5(a) and 5(b) shows the temporal evolution of $|\Delta T(\lambda_{peak}= 520$ nm, $t)|$ and $|\Delta R(\lambda_{peak}= 520$ nm, $t)|$ measured on the same samples. Here, the subscript *peak* denotes the maximum value of the NLO response in the spectral and temporal ranges studied. For a single Ag layer, the maximum $|\Delta T(\lambda, t_{peak})|$ and $|\Delta R(\lambda, t_{peak})|$ are at least an order of magnitude smaller (<0.5% for a pump fluence of 50 J/m^2) than those found in bilayer or single Au layer films [7], so their values are not included in Figure 4 and Figure 5. For bilayer films, **S1**, **S2**, and **S3**, the $\Delta T(\lambda, t_{peak})$ and $\Delta R(\lambda, t_{peak})$ spectra display similar dispersion characteristics found in a single Au layer (**R1**). Under the same incidence pump fluence, the peak-to-valley magnitude of $\Delta T(\lambda, t_{peak})$ and $\Delta R(\lambda, t_{peak})$ gradually reduces as the mass thickness ratio of Au to Ag decreases from **R1**, **S1**, **S2** to **S3** (Figure 4(a) and 4(b)). Interestingly, there is a consistent blue-shift of the wavelength at which maximum values of $\Delta T(\lambda_{peak}, t_{peak})$ and $\Delta R(\lambda_{peak}, t_{peak})$ are observed by decreasing the mass thickness ratio of Au to Ag, the $|\Delta T(\lambda_{peak}, t_{peak})|$, where peak wavelength and magnitude change from $|\Delta T(513$ nm, $t_{peak})|= 7.8\%$ for **R1** to $|\Delta T(498$ nm, $t_{peak})|= 4.8\%$ for **S1**, $|\Delta T(496$ nm, $t_{peak})|= 2.5\%$ for **S2**, and $|\Delta T(490$ nm, $t_{peak})|= 0.7\%$ for **S3**. A similar trend is found for ΔR as shown in Figure 4(b). The trend of these shifts is consistent with the shifts in the onset of interband transitions shown in Figure 1(a). This correspondence shows that both linear and NLO properties can be tuned by controlling the mass-thickness ratio between Ag and Au in bilayer films, albeit the magnitude of the NLO changes appears to be reduced as the Ag content increases. This apparent reduction, as will be later described, arises primarily from differences in the absorbed power within the Au layer.

19

2.3.2 Two-temperature model and temperature-dependent physical models of NLO properties

In order to gain a better understanding of the NLO properties of these bi-metal layers, the two-temperature model was introduced (Eq. 2-1) as follows to describe the heating of electrons and the lattice when optically pumped.

$$C_e(T_e)\frac{dT_e}{dt} = -G(T_e - T_l) + P(t)$$
$$C_l\frac{dT_l}{dt} = G(T_e - T_l)$$

(2-1)

The changes in electron and lattice temperatures, T_e and T_l, respectively, calculated through the two temperature model depend upon intrinsic material properties such as the electron and lattice specific heats, C_e and C_l, respectively, and the electron phonon coupling constant, G, and are driven by the density of absorbed power within each individual layer, $P(t)$. In our simulation, $C_e(T_e) = (62 \pm 5) \times T_e$ [J/m^{3}K], $C_l = (3.2 \pm 0.4) \times T_e$ [J/m^{3}K], $G = (1.8 \pm 0.1) \times 10^{16}$ [W/m^{3}K], and the density of absorbed power is estimated as $P(t) = I(t)A/d$ [W/m^3], where $I(t)$ is the pump irradiance, here assumed to have a Gaussian temporal profile with a pulse width of 60 fs (HW 1/e), A is the linear absorptance in the metal layer calculated using the transfer matrix method, and d is the thickness of the metal layer. These values were obtained by fitting $\Delta T(\lambda_{peak}, t)$ and $\Delta R(\lambda_{peak}, t)$, measured for an incident pump fluence of 8 J/m^2, with the physical model described in following paragraphs and show magnitudes that are comparable to literature values [6]. Here, note that the linear approximation of $C_e(T_e)$ and the temperature independent value of G are valid only in the low-fluence regime; this is, for electron

temperatures smaller than around 3000 K for Au [61]. At the highest pump fluence of 25 J/m^2 used in this work, the maximum electron temperature in all samples is calculated to be in 1300-1500 K.

The electron and lattice temperatures derived from the two-temperature model are used in a temperature-dependent physical model of the permittivity to calculate the complex refractive index changes $\Delta n_{sim}(\lambda, t)$ and $\Delta k_{sim}(\lambda, t)$.

For simplicity, the model implemented here to describe the NLO response of bilayers only accounts for the contribution of the Au component. This is motivated by the fact that only very minor adjustments were found when the contribution of Ag, as described by Owen, et al.[7], was included in the calculations. The permittivity of Au, was modeled as a set of explicit equations (Eqs. 2-1 ~ 2-4), as functions of frequency, temperature, and time, via a Drude-like intraband transition term (ε_{intra}) and the superposition of an interband transition term (ε_{inter}) following Bigot, et al. [62], as follows

$$\varepsilon\left(\omega, T_l\left(t\right), T_e\left(t\right)\right) = \varepsilon_{intra}\left(\omega, T_l\left(t\right), T_e\left(t\right)\right) + \varepsilon_{inter}\left(\omega, T_e\left(t\right)\right) \qquad (2\text{-}2)$$

Hereafter, ω is the free space optical frequency, t is the time, and $T_l(t)$ and $T_e(t)$ are temporal dependent lattice and electron temperatures, respectively.

For the first term in Eq. 2-2,

$$\varepsilon_{intra}\left(\omega, T_l\left(t\right), T_e\left(t\right)\right) = 1 + \varepsilon_b - \frac{\omega_p^2}{\omega^2 + i\gamma\omega}$$

with parameters, (2-3)

$$\gamma\left[T_l(t), T_e(t)\right] = \gamma_0 + \gamma_1 \times T_l(t) + \gamma_2 \times T_l^2(t) + \gamma_3 \times \omega^2$$

where, ε_b is the background dielectric constant, γ is the damping constant, ω_p is the bulk plasma frequency, and γ_0, γ_1, γ_2,and γ_3 are constant coefficients [7].

For the second term in Eq. 2-2,

$$\varepsilon_{inter}\left(\omega, T_e\left(t\right)\right) = \sum_{j=1}^{M} \kappa_{(j)} \int_0^\infty dx \frac{\sqrt{x - E_{g(j)}}}{x^2} \left[1 - F_{(j)}\left(x, T_e(t)\right)\right] \frac{\hbar^2\omega^2 - x^2 - \gamma_{ee(j)}^2 - 2i\hbar\omega\gamma_{ee(j)}}{(\hbar^2\omega^2 - x^2 - \gamma_{ee(j)}^2)^2 + 4\hbar^2\omega^2\gamma_{ee(j)}^2}$$

with parameters, (2-4)

$$F_{(j)}(x, T_e(t)) = \left(1 + \exp\left(\frac{x - E_{f(j)}}{k_B T_e(t)}\right)\right)^{-1}, E_{f(j)} = E_{fd(j)}\left(1 - \frac{\pi^2}{12}\left(\frac{k_B T_e(t)}{E_{fd(j)}}\right)^2\right),$$

and $\gamma_{ee(j)}[T_e(t)] = \hbar(\gamma_{a(j)} T_e^2(t) + \gamma_{b(j)}\omega^2)$

where the summation is composed of M interband terms and each contribution term is denoted by the subscript j, x is the electron energy, κ is a constant related to effective electron mass, E_g is the minimum transition energy from a valence band to an ideal parabolic conduction band, γ_{ee} is the inverse scattering time, $F(x, T_e(t))$ is the electron occupation number, E_f is the electron distribution function, E_{fd} is the transition energy from the d-band to the Fermi level, k_B is the Boltzman constant, $\hbar$ is the plank constant, and γ_a and γ_b are constant coefficients [62].

22

The value of the constant coefficients used in the Au permittivity model is listed in Table 1and Table 2. These values were obtained by fitting the measured steady-state permittivity at room temperature [63], $T_l(t) = T_e(t) = 300$ K, with Eqs. 2-2 ~ 2-4. Figure 6 shows the comparison between simulated Au permittivity and that obtained by spectroscopic ellipsometry.
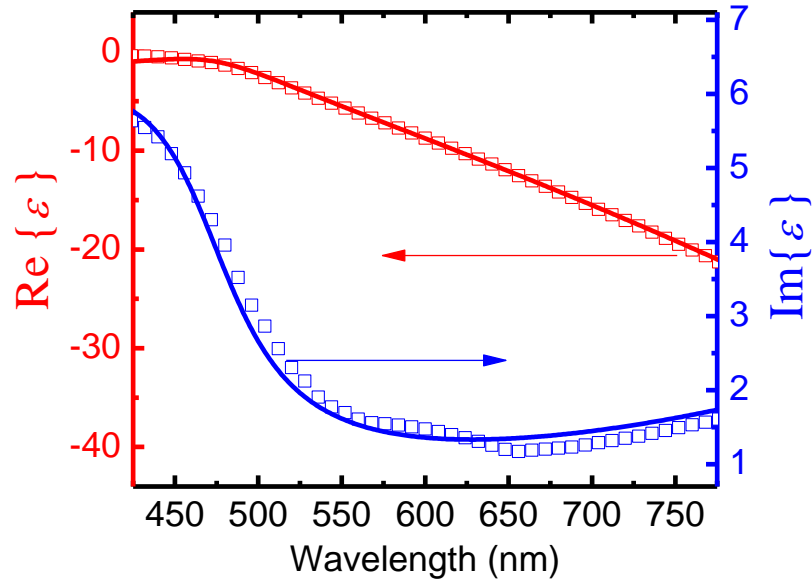
Figure 6: Comparison of measured (symbols) and simulated (solid lines) complex permittivity spectra in visible range for the fabricated sample R1. The permittivity of Au was modeled as a set of explicit equations (Eqs. 2-2 ~ 2-4) and compared with measured ellipsometric data.

Table 1: Constant coefficients of an Au permittivity model for intraband transition term (Eq. 2-3).

ε_{intra}	ε_b	$\gamma_0 (s^{-1})$	$\gamma_1 (s^{-1}k^{-1})$	$\gamma_2 (s^{-1}k^{-2})$	$\gamma_3 (s^{-3})$	$\omega_p (s^{-1})$
	3.5	1.2×10^{14}	1×10^{10}	2.5×10^{7}	2.1×10^{-18}	1.3×10^{16}

Table 2: Constant coefficients of an Au permittivity model of the first and second interband transition term (Eq. 2-4), respectively.

$\varepsilon_{inter(1)}$	$\kappa_{(1)}$	$E_{fd(1)}(eV)$	$E_{f(1)}(eV)$	$\gamma_{a(1)}(s^{-1}k^{-2})$	$\gamma_{b(1)}(s^{-3})$
	100	2.59	1.44	1.2×10^{-4}	1.6×10^{-16}
$\varepsilon_{inter(2)}$	$\kappa_{(2)}$	$E_{fd(2)}(eV)$	$E_{f(2)}(eV)$	$\gamma_{a(2)}(s^{-1}k^{-2})$	$\gamma_{b(2)}(s^{-3})$
	20	3.1	0.5	5.4×10^{-4}	7×10^{-17}

Simulated $\Delta T_{sim}(\lambda, t)$ and $\Delta R_{sim}(\lambda, t)$ are obtained by replacing N_{Au} with $N_{Au}(\lambda, t) = N_{Au} + \Delta N_{sim}(\lambda, t)$ (where $\Delta N_{sim}(\lambda, t) = \Delta n_{sim}(\lambda, t) + i\Delta k_{sim}(\lambda, t)$). Using this approach and without any further adjustment of the parameters in the model, $\Delta T_{sim}(\lambda, t)$ and $\Delta R_{sim}(\lambda, t)$ closely match with the experimental values. This comparison is shown in Figure 5(a) and 5(b), where a similar ultrafast temporal evolution is found for all samples. Although better fits could be obtained if small modifications to the value of the electron-phonon coupling rates are introduced to account for its temperature dependence and differences in sample morphology, the model here proposed is sufficient to describe the basic features of the NLO response measured in the bilayers.

In the proposed model, $\Delta N_{sim}(\lambda, t)$ is only ascribed to the Au layer. However, for potential applications in all-optical control devices it is useful to derive $\Delta N_{eff} = \Delta n_{eff} + i\Delta k_{eff}$ values which could be ascribed to the entire bilayer. Using a first order approximation, a Taylor expansion of ΔT and ΔR as functions of ΔN_{eff} yields the following system of linear equations

$$\Delta T = \frac{\partial T}{\partial n_{\text{eff}}} \Delta n_{\text{eff}} + \frac{\partial T}{\partial k_{\text{eff}}} \Delta k_{\text{eff}}$$

$$\Delta R = \frac{\partial R}{\partial n_{\text{eff}}} \Delta n_{\text{eff}} + \frac{\partial R}{\partial k_{\text{eff}}} \Delta k_{\text{eff}}$$

(2-5)

In solving this system, ΔN_{eff} is extracted from the experimental data. The partial derivatives, $\partial T/\partial n$, $\partial T/\partial k$, $\partial R/\partial n$ and $\partial R/\partial k$ were approximated by their differentials ($\Delta T/\Delta n_{\text{eff}}$, $\Delta T/\Delta k_{\text{eff}}$, and etc.) by introducing a small perturbation to N_{eff} in the entire bilayer.
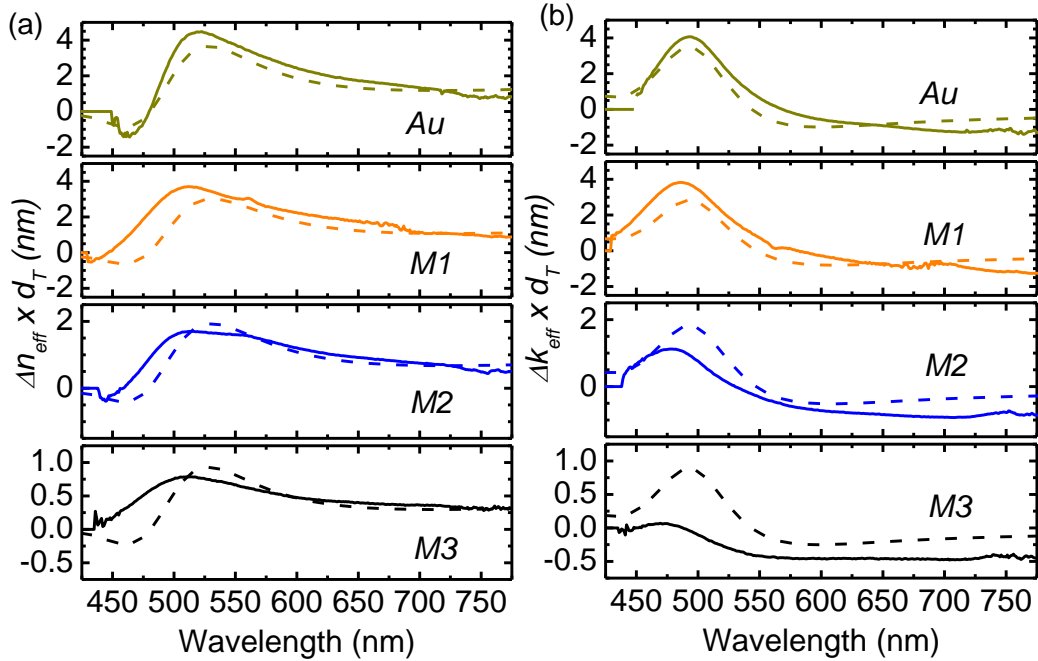
Figure 7: Spectral dependence of the (a) real and (b) imaginary optical path length change (ΔOPL) pumped at 560 nm with a fluence of 25 J/m² for Au (23 nm), *M1*, *M2*, and *M3*. Solid line is the extracted ΔOPL= $\Delta N_{\text{eff}} d_T$ and the dashed line is the simulated ΔOPL= $\Delta N_{\text{sim}} d_{Au}$ probed at the peak transmittance delay time.

Here it is worth pointing out that while it is tempting to establish a direct comparison between ΔN_{eff} and ΔN_{sim}, this is not straight forward. Because in calculating ΔN_{eff} and ΔN_{sim}, the change of refractive index is assumed to occur in layers with different thicknesses, ΔN_{sim} is related only to the thickness of the Au layer (d_{Au}) in the bilayer

structure, while ΔN_{eff} is ascribed to the total bilayer thickness (d_T). With these limitations in mind, a comparison can still be made if the change in optical path length (ΔOPL$=$ $\Delta N_{\mathrm{eff}}d_T$ or ΔOPL$= \Delta N_{\mathrm{sim}}d_{Au}$) is used. Figure 7 shows this comparison. In general, good order-of-magnitude estimations of ΔOPL and qualitatively good spectral agreement are obtained using both models. Spectral differences are ascribed to differences in the linear models used. Finally, due to the thermal nature of the NLO response observed in these bilayer films, $\Delta N_{\mathrm{eff}}(520\ \mathrm{nm})d_T$ does not follow a linear dependence on the absorbed pump fluence as shown in Figure 8. This trend is consistent with the nonlinear dependence of the electron temperature on the absorbed pump fluence. Furthermore, even at the same absorbed power, the NLO response of a single Au (23 nm) layer is larger than any of the bilayers *M1*, *M2*, and *M3*.
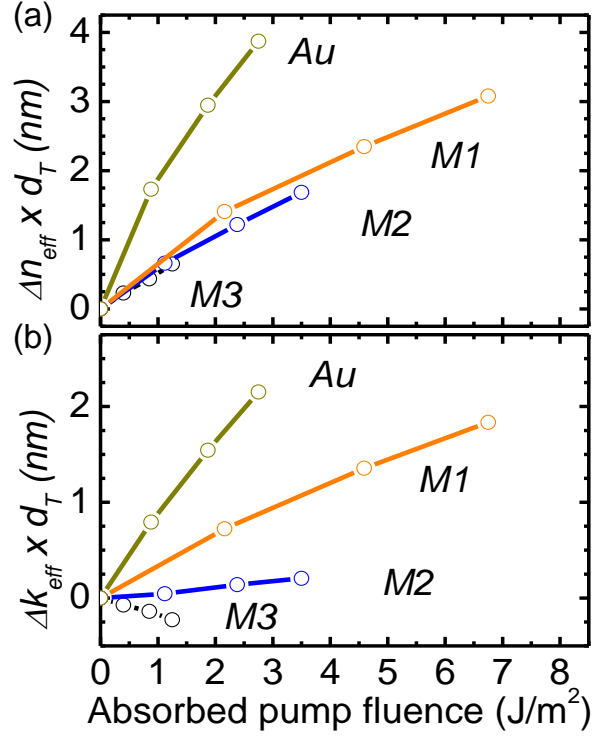
Figure 8: Absorbed pump fluence dependence of (a) real and (b) imaginary optical path length change (ΔOPL = ΔN$_{eff}$d$_T$), where ΔOPL(λ = 520 nm) is extracted at the peak transmittance change delay time and pumped at 560 nm for Au (23 nm), M1, M2 and M3.

2.4 Conclusion

The optical properties of Ag/Au bilayer metallic thin films with a total thickness of approximately 20 nm and with different Ag/Au mass-thickness ratios were studied. The effective refractive index values were found to be spectrally tunable by controlling the mass-thickness ratio between Au and Ag. Hence, the optical loss introduced by interband transitions in Au layers can be reduced. As a consequence, improvement of the quality factors (Q_{LSP} and Q_{SPP}) derived for plasmonic applications and the potential transmittance (Ψ) for optical filter applications are calculated within the visible range. These spectral shifts also lead to similar spectral shifts on the NLO response of the bilayers. The NLO response is shown to be ultrafast and comparable in origin and magnitude to that observed in single Au films. The NLO response in the bilayer films is dominated by the

ultrafast dynamics of the thermal exchange between the absorbed optical field and the electron cloud and the lattice in the Au layer. The combined properties of these bilayers could therefore be attractive for a variety of linear and nonlinear photonic applications.

The results in CHAPTER 2 have been published in the journal Optics Express: J. Hsu, C. Fuentes-Hernandez, A. R. Ernst, J. M. Hales, J. W. Perry, and B. Kippelen, "Linear and nonlinear optical properties of Ag/Au bilayer thin films," Opt. Express **20**, 8629-8864 (2012) [64].

CHAPTER 3: NOBLE METAL NONLINEAR OPTICAL DEVICES WITH ADJUSTABLE SPECTRAL AND ANGULAR BANDWIDTHS FOR ALL-OPTICAL CONTROLS AT VISIBLE WAVELENGTHS

3.1 Broadband NLO Device

3.1.1 Fabrication and characterization

All thin films were deposited on VWR Micro Slides glass substrates with a Kurt. J Lesker Axxis electron beam deposition system. Substrates were cleaned ultrasonically in deionized water, acetone and isopropanol for 15 min each. The films were deposited under vacuum at a pressure of 8.6×10^{-7} Torr (1.1×10^{-4} Pa) with a rotating sample holder that actively cools the substrates to room temperature. The Ag, Au, and SiO_2 were deposited at a rate of 0.2 nm/s, 0.05 nm/s, and 0.2 nm/s, respectively, monitored by crystal sensors.
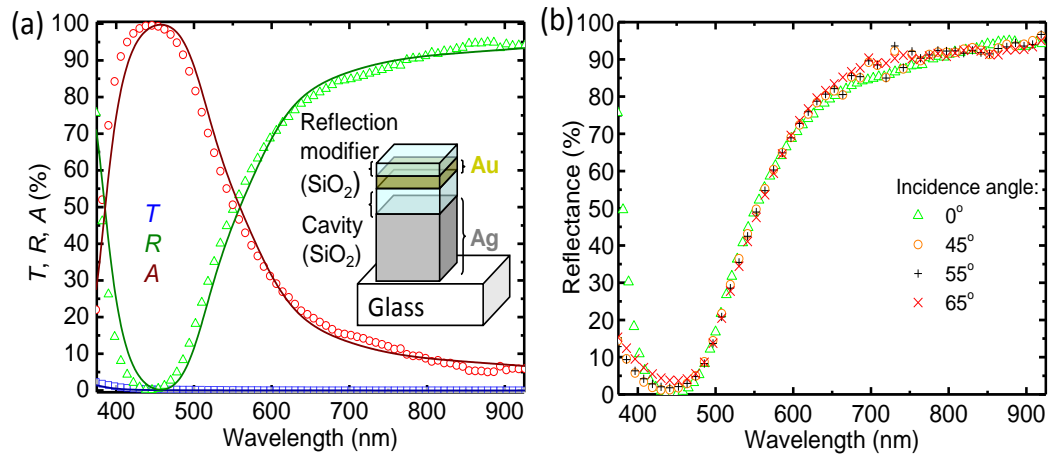
Figure 9: (a) Comparison of measured (symbols) and simulated (lines) transmittance (T, blue), reflectance (R, green), and absorptance (A, red) spectra in the visible range of the fabricated Broadband NLO Device sample. The inset shows the generalized thin film structure of the NLO device. (b) Measured reflectance spectra at varied incidence angles.

The inset of Figure 9(a) shows a generalized thin film structure of the **Broadband NLO Device**. It was fabricated by deposition of the Ag layer onto a glass substrate followed by the deposition of the Au layer sandwiched and protected by SiO_2 thin films with the following geometry:

Broadband NLO Device: Glass/Ag(100 nm) /SiO_2(81 nm)/Au(23 nm)/SiO_2(81 nm).

The layer thicknesses (shown inside the parentheses) were set to optimize the linear spectral and angular bandwidths while maintaining a maximum nonlinear reflectance change. Figure 9(a) shows the comparison between measured values of the transmittance (*T*), reflectance (*R*), and absorptance (*A*) spectra taken by a Shimadzu UV-Vis-NIR scanning spectrophotometer and the simulated spectra by transfer matrix method. The good match simultaneously verifies both the fabrication process and the simulation of the transfer-matrix method. Spectroscopic ellipsometric (SE) data (J.A. Woollam M-2000UI) were taken on individual films to determine the optical properties of each layer. The refractive indices ($N = n + ik$) of all films were calculated from SE data imposing Kramers-Kronig consistency to the calculated values. In addition, the spectroscopic ellipsometry also measures the reflectance spectra at varied angles shown in Figure 9(b) to determine the angular bandwidth of the sample.

The nonlinear optical properties (NLO) of the **Broadband NLO Device** were characterized by a commercially available white-light continuum (WLC) pump-probe spectroscopy system (Helios, ultrafast system). The pump pulse was tuned to a wavelength of 550 nm with a pulse width of 60 fs half-width-1/e (HW 1/e) and a spot size of 347 μm (HW 1/e) at the sample position, measured using a knife-edge scan. The WLC (420-950 nm) probe pulse had a spot size of 80 μm (HW 1/e) at the sample position and a low enough fluence to produce no observable NLO response in the sample. The total instrument response time is 150 fs full-width-half-maximum (FWHM). Because the

probe spot size is smaller, it is assumed that the probe overlaps with a region of approximately constant peak fluence from the pump. After averaging over one thousand probe pulses at each time delay, the change in optical density ($\Delta OD(\lambda, t)$) was recorded as a function of wavelength (λ) and delay time (t). The reflectance change spectra ($\Delta R(\lambda, t)$) of the WLC probe pulses were calculated from measured $\Delta OD(\lambda, t)$ for a variety of pump fluences by $\Delta R(\lambda, t) = R_0(\lambda) \cdot \left(10^{\Delta OD(\lambda,\, t)} - 1\right)$, where $R_0(\lambda)$ is the measured linear reflectance spectrum.

3.1.2 Linear optical properties

The structure of the **Broadband NLO Device** shown in the inset of Figure 9(a) can be seen as a Fabry-Perot filter consisting of a central dielectric layer (cavity) sandwiched by two reflectors; the first one is the thick Ag layer and the second one is the thin Au layer covered by a dielectric layer (reflection modifier) on top. This structure can provide a wide variation of absorptance values by varying the thickness distribution of its two dielectric layers.
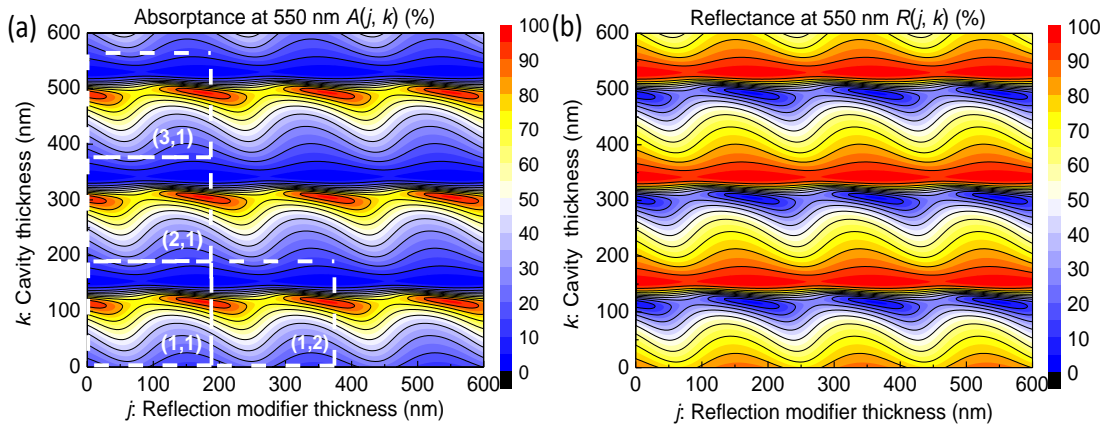
Figure 10: Simulated (a) absorptance $A(j, k)$ and (b) reflectance $R(j, k)$ at 550 nm of the general NLO device structure (shown in the inset of Figure 9) with different thickness combinations of reflection modifier (j) and cavity (k) layers.

Figure 10(a) shows a contour plot of absorptance $A(j, k)$ values as a function of the thickness j of the top dielectric layer which is called the reflection modifier, and the thickness k of the dielectric layer sandwiched between the two metal layers and which is referred to as the cavity thickness. The absorptance $A(j, k)$ was simulated using the transfer-matrix method at a wavelength of 550 nm. The structure can provide a wide variation of absorptance values, ranging from 2% to 96%. These variations are periodic with respect to the thicknesses of the reflection modifier and cavity layers, as can be seen from regions [(1,1), (2,1), (3,1), (1,2)] in Figure 10(a). Not surprisingly, in both directions these regions have a length of 188 nm corresponding to the half-wave optical thickness of SiO_2 at 550 nm[60]. As also indicated in Figure 10(a) and 10(b), the simulated reflectance is complementary to the absorptance at 550 nm (as expected from the negligible transmittance at this wavelength) and therefore shares the same periodicity.

The dominant contribution to the total absorptance of the **Broadband NLO Device** (55%) is primarily attributed to the Au thin film (53%), with negligible absorption in its component Ag layer (2%). This is in part because of the electric field distribution imposed by the NLO device geometry, and in part because Au is highly absorptive at wavelengths close to the interband transition onset, in the middle of the visible spectral range. On the other hand, the interband transition onset of Ag located in the ultraviolet (UV) spectral range causes light with photon energy far below the onset to be mostly reflected. The SiO_2 films are lossless based on SE data.

To illustrate the proposed approach, the **Broadband NLO Device** was designed to have a linear absorptance of 55% and a linear reflectance of 45% at 550 nm. This choice was arbitrary, but it is limited by a trade-off between the linear reflectance and the strength of the NLO response of a NLO device. Although both properties are preferred in general all-optical control applications, a compromise was made here to pick up the **Broadband NLO Device**. The trade-off is because that a higher linear absorptance (A) drives the stronger nonlinearity of the **Broadband NLO Device**, on the other hand, it

32

also decreases the linear reflectance (R), which is expected because R and A spectra are complementary in the whole visible spectral range as shown in Figure 9(a). The measured R spectrum also shows that the fabricated **Broadband NLO Device** sample is a long wavelength pass optical filter with a broad spectral bandwidth. In addition, the measured R spectrum as a function of angle of incidence in Figure 9(b) is shown to be angularly insensitive. Within incidence angles up to 65˚, the R spectrum barely changes compared to the normal incidence. The linear optical response of the **Broadband NLO Device** shows both broad spectral and angular bandwidth.

3.1.3 Nonlinear optical properties

In the **Broadband NLO Device** structure, as the linear absorption in the Au thin film is increased, the thermal nonlinearity of this layer is enhanced and consequently the NLO response of the NLO device. To illustrate this, simulations of the refractive index change have been carried out on Au using the two-temperature model and a physical model describing the permittivity as previously shown in CHAPTER 2. In short, the linear absorptance in the Au film is calculated using the transfer-matrix method. The absorbed optical power density is introduced as the source term in the two-temperature model. The electron and lattice temperatures derived through this model are used to calculate a temperature-dependent permittivity function. The refractive index of the metal, before and after optical excitation is taken as the root-square of the modeled permittivity.
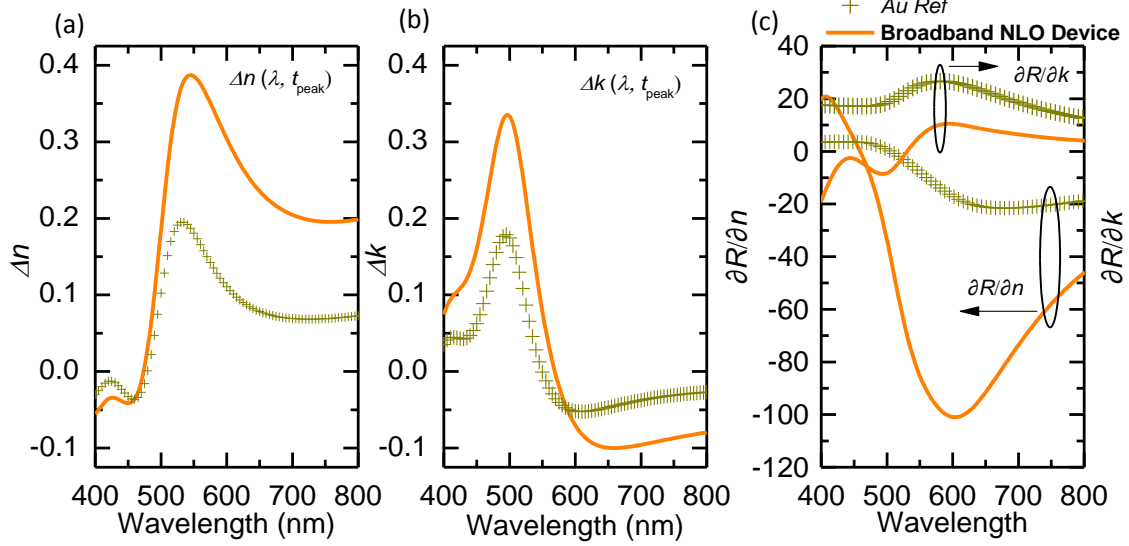
Figure 11: Spectral comparison of simulated (a) real and (b) imaginary refractive index changes between the 23 nm-thick Au film inside the Broadband NLO Device (orange lines) and a 23 nm-thick Au film on a glass substrate (*Au Ref*) (dark yellow symbols). Simulations were shown for an incident peak irradiance of 13 GW/cm^2 at 550 nm. (c) Spectral comparison of simulated $\partial R/\partial n$ and $\partial R/\partial k$ for the same Au containing structures.

Figure 11(a) and 11(b) show the simulated refractive index changes ($\Delta N_{Au}(\lambda, t_{peak})$ = $\Delta n(\lambda, t_{peak}) + i\Delta k(\lambda, t_{peak})$) in the visible spectra for a 23 nm-thick Au film on a glass substrate (*Au Ref*) and the **Broadband NLO Device** with the same thickness of the Au layer, assuming a pump pulse fluence of 16 J/m^2 (peak irradiance 13 GW/cm^2) at 550 nm. Here, t_{peak} denotes the delay time of the probe pulse that yields maximum NLO response in the temporal ranges studied. Note that the peak wavelength of $\Delta n(\lambda, t_{peak})$ and $\Delta k(\lambda, t_{peak})$ are always located around the interband transition onset of Au at 520 nm. For the **Broadband NLO Device**, the peak-to-valley magnitude of Δn and Δk doubles. This is achieved by increasing the linear absorptance at 550 nm in the Au thin film from 19% for *Au Ref* to 53% in the **Broadband NLO Device**.

The correspondent reflectance changes as a function of wavelength (λ) and delay time (t) can also be calculated by the following Eq. 3-1.

$$\Delta R(\lambda,t) = R(N_{Au}(\lambda) + \Delta N_{Au}(\lambda,t)) - R_0(\lambda) \tag{3-1}$$

where $R(N_{Au}(\lambda)+\Delta N_{Au}(\lambda, t))$ and $R_0(\lambda)$ are the simulated reflectance after and before a pump pulse excitation, $N_{Au}(\lambda)+\Delta N_{Au}(\lambda, t)$ is the refractive index values of 23 nm Au after optically pumping, $N_{Au}(\lambda)$ is the linear refractive index, and $\Delta N_{Au}(\lambda, t)$ is the simulated nonlinear refractive index change ($\Delta N_{Au}(\lambda, t) = \Delta n(\lambda, t) + i\Delta k(\lambda, t)$). Since the thermal nonlinearity of Ag is order of magnitudes smaller compared to Au, for the **Broadband NLO Device**, $\Delta R(\lambda, t)$ is assumed arising only from $\Delta N_{Au}(\lambda, t)$ of the Au component.

Although the reflectance changes $\Delta R(\lambda, t)$ can be calculated exactly and have been used in the optimization process while designing the **Broadband NLO Device**, developing a simplified analysis is attractive to illustrate the enhancement mechanism of ΔR. For example, the measured $\Delta R(550$ nm, $t_{peak})$ increases from -1% for *Au Ref* to -16% for the **Broadband NLO Device** excited by a peak pump irradiance 13 GW/cm^2 at 550 nm. Hence, the first order approximation to the Taylor expansion of ΔR is taken as functions of ΔN_{Au} and yields the following equation.

$$\Delta R = \frac{\partial R}{\partial n}\Delta n + \frac{\partial R}{\partial k}\Delta k \approx \frac{\partial R}{\partial n}\Delta n \qquad\qquad (3\text{-}2)$$

The partial derivatives, $\partial R/\partial n$ and $\partial R/\partial k$, were approximated by their differentials ($\Delta R(N_{Au} + \Delta n)/\Delta n$ and $\Delta R(N_{Au} + \Delta k)/\Delta k$), introducing a small perturbation to N_{Au} in the linear model used to calculate R. Eq. 3-2 is only valid for small values of ΔN_{Au}. The simplification of Eq. 3-2 into a one term equation comes about since at the wavelength 550 nm, Figure 11(b) shows that $\Delta k(550$ nm, $t_{peak})$ values for the **Broadband NLO Device** and *Au Ref* are both close to zero, and from 515 nm to 800 nm the calculated $\partial R/\partial n$ for the **Broadband NLO Device** is always at least ten times larger than $\partial R/\partial k$, as shown in Figure 11(c). Hence, ΔR can be decomposed into two components: Δn and

$\partial R/\partial n$. The first term, Δn, is an intrinsic property of the nonlinear material, although is dependent on the absorbed optical power as has been shown in Figure 11(a) and 11(b).

In Figure 11(c), the **Broadband NLO Device** generally displays higher $\partial R/\partial n$ values than the *Au Ref* in the visible spectral range. For instance, at 550 nm, $\partial R/\partial n$ improves from a value of -8 for the *Au Ref* to a value of -85 for the **Broadband NLO Device**. Note that the **Broadband NLO Device** not only doubles the Δn of the Au film due to an increased linear absorptance from 19% for *Au Ref* to 53% in the **Broadband NLO Device**, but also introduces a better structural design which improves the sensitivity of R to small changes on the real part of the refractive index of Au. In contrast, the device structure reduces the sensitivity of R to changes in the imaginary part of the refractive index of Au; as revealed by the smaller values of $\partial R/\partial k$ found for the device structure than for *Au Ref*. As calculated by Eq. 3-2, ΔR is expected to improve by around 20 times compared to *Au Ref*. This evaluation was verified by the measured $\Delta R(550 \text{ nm}, t_{peak})$, which increases 16 times from *Au Ref* to the **Broadband NLO Device**.

It is interesting to note that, spectrally, the maximum magnitude of $\partial R/\partial n$ is not at 550 nm, where it reaches a magnitude of -85, but instead at 600 nm, where it reaches a magnitude of -101. This is even though the **Broadband NLO Device** was designed for degenerate pump-probe operation, which means that $\Delta R(550 \text{ nm})$ was maximized for this geometry. Note that if the **Broadband NLO Device** is excited and probed at 600 nm, a smaller magnitude of ΔR is expected than the value when excited at 550 nm. This is because the linear absorption at 600 nm is only 31%; much smaller than the 55% obtained at 550 nm. Hence, differences in Δn between excitation at 550 nm and at 600 nm, $\Delta n(550 \text{ nm}) \gg \Delta n(600 \text{ nm})$, are expected to be more significant than the difference in $\partial R/\partial n$ found at these wavelengths.

In addition, note that most $\partial R/\partial n$ values in Figure 11(c) of **Broadband NLO Device** are negative with positive Δn values in Figure 11(b) across the visible spectral range. The total product of ΔR values calculated by Eq. 3-2 shows that the general

characteristic of ΔR is negative. After the **Broadband NLO Device** is pumped optically, positive Δn values will cause a redistribution of the electric field throughout the structure. These changes in the electric field distribution lead to a larger field within the Au layer, resulting in an increase of absorptance. Since reflectance and absorptance of the **Broadband NLO Device** are complementary, an increase in absorptance (ΔA) will lead to a decrease in reflectance (ΔR).

3.1.4 Optimization and design process of broadband NLO device
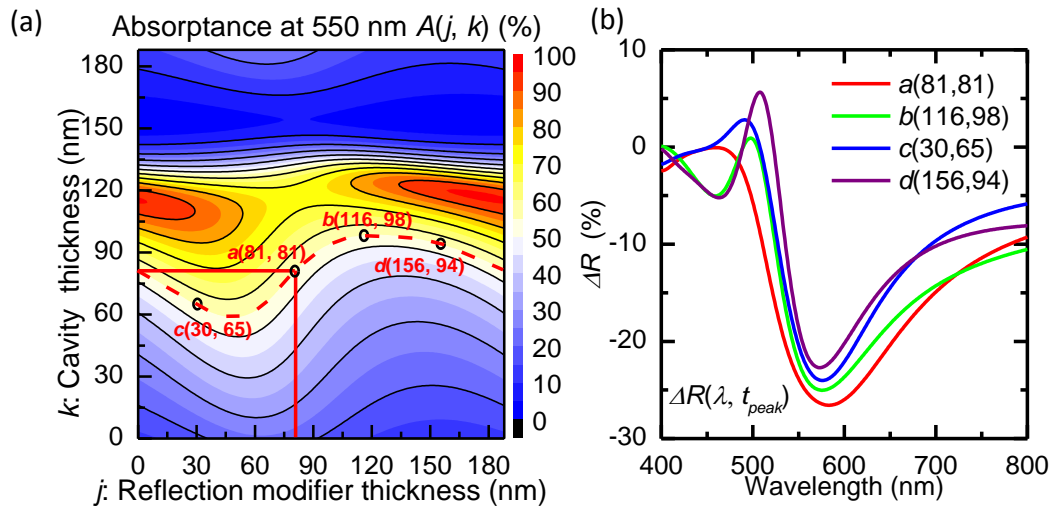
Figure 12: (a) Absorptance $A(j,k)$ at 550 nm of the Broadband NLO Device with different thickness combinations of reflection modifier (j) and cavity (k) layers within the region (1,1) defined in Figure5(c). The red line represents all thickness combinations leading to $A(j,k)$ =55%. Points a(81,81), b(116,98), c(30, 65), and d(156,94) represent four different illustrative thickness combinations used for the evaluation of $\Delta R(\lambda, t_{peak})$. Numbers inside the parenthesis are thicknesses given in nm. The point a(81,81), highlighted, corresponds to the fabricated Broadband NLO Device. (b) Reflectance changes ΔR of the selected mirror combinations.

Here, the optimization process for designing the thickness distribution of the **Broadband NLO Device** is explained in detail. Although a higher linear absorptance (A) on the **Broadband NLO Device** leads to stronger NLO changes in the Au layer, the trade-off is that the linear reflectance (R) is also reduced. Arbitrarily, the **Broadband NLO Device** was set to have a linear absorptance (A) of 55% and a reflectance (R) of 45% at 550 nm.

As discussed, the periodicity of R and A on the reflection modifier (j) and cavity (k) thicknesses allows the optimization processes to be conducted only on the region designated (1, 1). Figure 12(a) shows the $A(j, k)$ of the region (1, 1) and a red dashed line indicates all thickness combinations which would fit the design criterion of $A(j, k) = 55\%$. Four different dielectric layer thickness combinations (j, k), a(81, 81), b(116, 98), c(30, 65), and d(156, 94), were picked as examples to illustrate the design process. The units of the thicknesses denoted inside the parenthesis have been dropped for convenience. This process required calculations of $\Delta R(\lambda, t_{peak})$ for multiple structures along this line in order to estimate the structure that maximized $\Delta R(550 \text{ nm}, t_{peak})$.

Figure 12(b) shows the $\Delta R(\lambda, t_{peak})$, calculated by Eq. 3-1 using the values of $\Delta N_{Au}(\lambda, t_{peak})$ shown in Figure 11(a) and 11(b), at the peak response time, t_{peak}, for the **Broadband NLO Device** structures excited at 550 nm. The results show that $\Delta R(550 \text{ nm}, t_{peak})$ improves gradually from points d(156, 94) through a(81,81) and starts decreasing from a(81,81) to c(30, 65). The maximum magnitude of $\Delta R(550 \text{ nm}, t_{peak})$ was found to be located at a(81, 81). As expected, the value of $\Delta R(550 \text{ nm}, t_{peak})$ was found to be the same in other regions provided that the dielectric thicknesses were increased by half-wave optical thickness of SiO_2 at 550 nm.

3.1.5 Pump-probe experiments
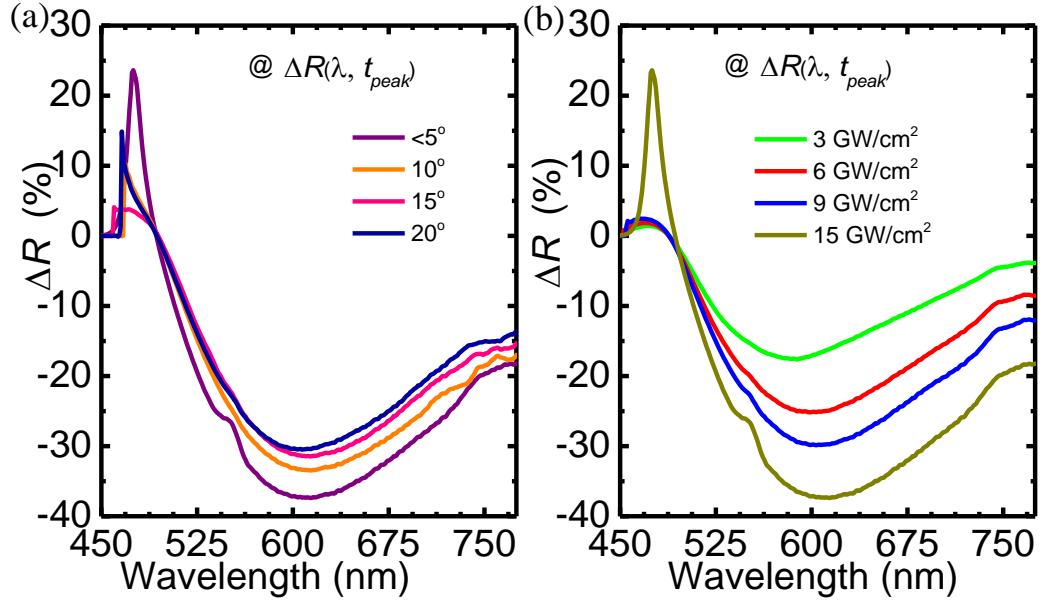
Figure 13: Reflectance changes (ΔR) of the Broadband NLO Device pumped at 550 nm of (a) spectral spectrum $\Delta R(\lambda, t_{peak})$ with respect to different incidence angles of <5° (purple line), 10° (orange line), 15° (pink line), and 20° (dark blue line); (b) $\Delta R(\lambda, t_{peak})$ at the peak response time t_{peak}, and (c) temporal dependence $\Delta R(600$ nm, $t)$ at probe wavelength 600 nm for different peak pump irradiance 10 (green line), 21 (red line), 31 (blue line) and 51(dark yellow line) GW/cm^2.

Figure 13(a) shows that angular dependence of $\Delta R(\lambda, t_{peak})$ measured in pump-probe experiments conducted on the **Broadband NLO Device** at a pump irradiance of 51 GW/cm^2 at 550 nm. Here, t_{peak} denotes the maximum magnitude of ΔR in the temporal ranges studied. As expected from our simulations, $\Delta R(\lambda, t_{peak})$ displays a broad spectral and angular bandwidth. For instance, for angles < 20° it was found that $\Delta R(\lambda, t_{peak})$ across the visible spectral range changes by no larger than 7% with respect to data acquired near normal incidence (< 5°).

Error! Reference source not found.(b) shows the values of $\Delta R(\lambda, t_{peak})$ easured for peak pump irradiances of 10, 21, 31, and 51 GW/cm^2 at 550 nm. For increasing pump irradiance, $\Delta R(\lambda, t_{peak})$ spectra consistently displays broad spectral bandwidth characteristics. It was confirmed that the highest irradiance did not damage the sample by acquiring multiple data sets at high and low irradiance levels on the same spot. For potential applications in all-optical devices, it is useful to derive the irradiance

evolution of the absolute reflectance calculated by $R_0(\lambda) + \Delta R(\lambda, t_{peak})$, where $R_0(\lambda)$ is the measured linear reflectance shown in Figure 9(a).
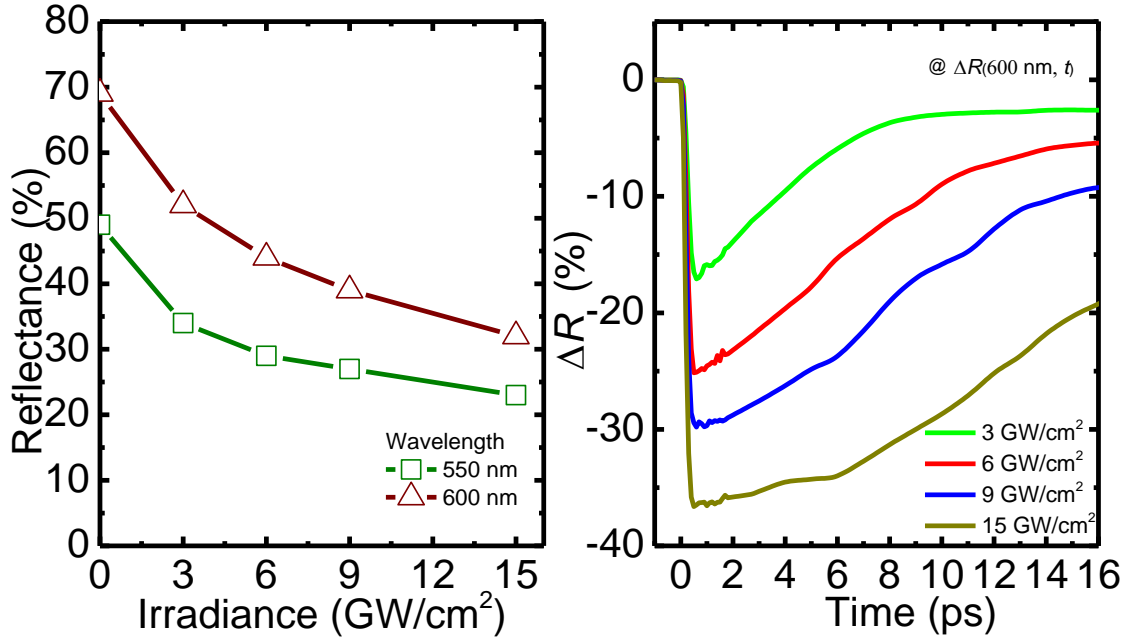
Figure 14: (a) Irradiance dependent reflectance (%) at 550 nm (dark green line and symbol) and 600 nm (dark red line and symbol) by adding linear reflectance $R_0(\lambda)$ with measured $\Delta R(\lambda, t_{peak})$ at the peak response time t_{peak}, and (b) temporal dependence $\Delta R(600\ nm, t)$ at probe wavelength 600 nm for different peak pump irradiances of the Broadband NLO Device sample pumped at 550nm.

Figure 14(a) shows that the **Broadband NLO Device** offers significantly strong reflectance suppression from a reasonably high $R_0(\lambda)$, such as from 49% to 23% at 550 nm and from 69% to 32 % at 600 nm by increasing pump irradiance to 51 GW/cm². Overall, the power dependent reflectance of the **Broadband NLO Device** can meet multiple engineering requirements in the visible spectral range by having an extreme large magnitude of ΔR, ultrafast response, and fairly broad spectral and angular bandwidths.

Finally, Figure 14(b) shows the temporal evolution of $\Delta R(600\ nm, t)$ as a function of the peak pump irradiances. Here, the peak wavelength has been selected to illustrate the ultrafast temporal evolution of the NLO response of the **Broadband NLO Device**. For increasing peak pump irradiance, $\Delta R(600\ nm, t)$ shows a larger magnitude and a

delayed relaxation of the reflectance modulation. A very similar behavior has been reported in single Au films [18, 48, 65], and has been attributed to a change of the electronic specific heat with increased temperature.

3.2 Narrowband NLO Device
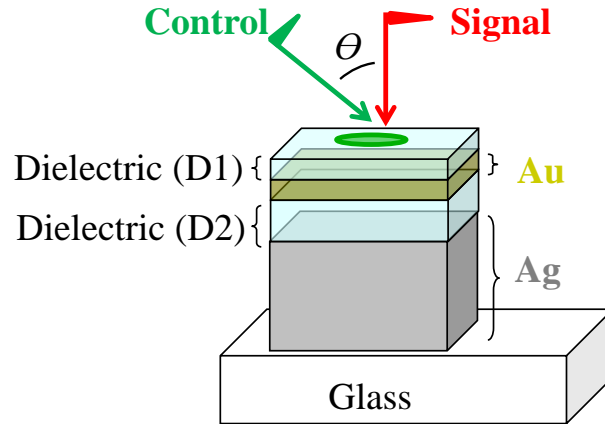
Figure 15: Non-collinear beam geometry imposed on the NLO device with a signal pulse at the normal incidence and a control pulse at the angle of incidence Θ.

The challenge for producing maximum reflectance changes in the **Broadband NLO Device** structure is limited by the trade-off between its linear reflectance (R) and reflectance change (ΔR) as discussed before. In short, an absorbed laser pulse in the **Broadband NLO Device** structure drives a thermal nonlinearity of the Au layer and consequently the NLO response of the whole structure. Note that if the linear absorptance (A) is increased such that the NLO device produces a larger ΔR, this increased A also leads to a reduced R; an undesirable optical signal loss in all-optical control applications. The present study mitigates this inherent constrain by imposing a non-collinear beam geometry on the same four layer NLO device structure as shown in Figure 15.

Figure 15 shows a generalized thin-film structure, comprising of a 100 nm-thick Ag and a 23 nm-thick Au sandwiched between two dielectric layers such as D1 and D2. This four-layer thin-film structure is used in **Broadband NLO Device**, which provides

41

large reflectance changes in response to a high peak-power optical pulse. The **Broadband NLO Device** represents a conventional all-optical control in the sense that it allows a low peak-power signal pulse to be modulated in amplitude and phase by a high peak-power control pulse. The **Broadband NLO Device** is operated using a nearly collinear beam geometry (Ex: $\Theta = 0°$ in Figure 15), where both signal and control pulses are traveling nearly or at the same incidence angle. In contrast, the **Narrowband NLO Device** shown in Figure 15 is designed to operate in a non-collinear beam geometry, wherein the high angular dependence is designed such that the control pulse experiences a high linear absorptance at a first angle of incidence Θ, and the signal pulse experiences a low linear absorptance at a second angle of incidence (i.e. the normal incidence). In other words, the **Narrowband NLO Device** presents a highly angularly dependent linear absorptance (A). This four layer structure with a high angular A dependence is proposed to maximize the linear absorptance of the control pulse, which leads to accessing the maximum NLO response of the device, but simultaneously limits the loss experienced by the signal; thus offering a better compromise between NLO response and linear loss than the **Broadband NLO Device**.

It is interesting to note that since the linear absorptance at the normal incidence is small, even a high peak-power signal pulse at the normal incidence does not cause a large NLO response in the **Narrowband NLO Device**. The engineered angularly dependent absorptance consequently enables a selective excitation of the NLO response by a control pulse but simultaneously suppresses the excitation from a signal pulse itself. Conventional all-optical control, without such angular sensitivity, is commonly limited in this aspect because a strong signal pulse will lead to undesired self-modulation. The proposed **Narrowband NLO Device** aims to show a high angular sensitivity in its NLO response, which can open up a new type of all-optical control for high peak-power signal pulses, for example, laser material processing applications such as laser manufactures and pulsed-laser surgeries.

42

3.2.1 All-optical controls of high peak power signal pulses

All-optical controls have been primarily applied in the context of optical signal processing applications because advantages offered by its ultrafast operation, as shown in a variety of devices [66] such as all-optical switch, all-optical modulator, and all-optical logic gate. These devices use nonlinear optical (NLO) materials to modulate the amplitude and phase of one light beam (signal) through their NLO properties by the other light beam (control). Different types of NLO properties such as Kerr nonlinearity [38, 67], and saturable absorption [68] have been used for all-optical control applications. However, a common inherent limitation of all these approaches is that the peak power of the controlled signal beam needs to be weaker than a control beam to selectively excite the NLO response of the material.

Andrew M. C. Dawes *et al.*[69] have overcome some aspects of this limitation by using a highly sensitive light-induced scattering in a warm laser-pumped rubidium (Rb) vapor. In contrast to conventional all-optical controls, a weak control light is sufficient to redirect other strong signal lights. This approach opens up new possibilities for all-optical devices to be cascaded and single-photon excitable. It needs to be noted that both signal and control lights here were using continuous wave (CW) lasers rather than pulsed lasers as extensively discussed in this dissertation. This new all-optical control operates within the so-called low-light-level regime, and has been achieved by other methods as well [70]. However, several drawbacks exist when exploiting the NLO response of atomic vapors, since they require a complex optical wave-mixing set up to drive intensive lights and atoms interactions in NLO vapors. In addition, the dynamic of the optical wave-mixing is also orders-of-magnitudes slower than ultrafast NLO processes such as Kerr nonlinearities or ultrafast thermal nonlinearities of metals. The speed of the all-optical control by Rb vapors has a rising time up to 4 µs, limited by its ground-state optical pump time.

On the other hand, the large NLO properties of noble metal thin films (Ex: Ag, Au, and Cu) are relatively easier to excite using the absorption of a single ultrafast optical pulse. The absorbed energy and power of an optical pulse (control pulse) arises electron and lattice temperatures of a metal thin film, then smears the electronic distribution of the metal around the Fermi energy level (Fermi-smearing), and causes a large and ultrafast change of transmittance and reflectance on the other pulse (signal pulse) at visible wavelengths [64]. As an example of this approach, a metal-dielectric thin-film structure (**Broadband NLO Device**) was developed. This structure amplifies the ultrafast NLO properties for an Au thin film and consequently enhances the NLO response of the whole Au based thin film structure.

3.2.2 Fabrication and characterization

A NLO device with a high angular dependence was designed using the theoretical formalism presented in Section 3.1.4 and fabricated by deposition of the Ag layer onto a glass substrate followed by the deposition of the Au layer sandwiched and protected by ZrO_2 thin films with the following geometry:

Narrowband NLO Device: Glass/Ag(100 nm)/ZrO_2(389 nm)/Au(23 nm)/ZrO_2(133 nm).

All thin films were deposited on VWR Micro Slides glass substrates with a Kurt. J Lesker Axxis electron beam deposition system. Substrates were cleaned ultrasonically in deionized water, acetone, and isopropanol for 15 min each. The films were deposited under vacuum at a pressure of 5×10^{-7} Torr (6.7×10^{-5} Pa) with a rotating sample holder that actively cools the substrates to room temperature. The Ag, Au, and ZrO_2 were deposited at a rate of 0.2 nm/s, 0.05 nm/s, and 0.2 nm/s, respectively, monitored by crystal sensors. The combination of layer thicknesses (shown inside the parentheses) was chosen to have a high angular dependence on its linear reflectance.

Reflectance spectra ($R(\lambda, \Theta)$) were measured at visible wavelengths for the NLO device sample, where λ is the wavelength, and Θ is the angle of incidence. $R(\lambda, \Theta = 0°)$ was taken by a Shimadzu UV-Vis-NIR scanning spectrophotometer, and $R(\lambda, \Theta = 45°)$ was taken by a J.A. Woollam M-2000UI spectroscopic ellipsometry. The NLO properties were characterized by a commercially available white-light (WLC) continuum pump-probe spectroscopy system (HELIOS, ultrafast system), described in detail in reference [64]. In short, a pump pulse (presenting as a control pulse in Figure 15) was tuned to a wavelength of 568 nm with a pulse width of 60 fs half-width-1/e (HW 1/e) and a beam radius of 420 μm (HW 1/e) at the sample position, measured using a knife-edge scan. The WLC (420 - 950 nm) probe pulse (representing as a signal pulse in Figure 15) had a beam radius of 80 μm (HW 1/e) at the sample position and a low enough peak irradiance to produce no observable NLO response in the sample. The total instrument response time is 150 fs full-width-half-maximum (FWHM). Because the probe beam radius is smaller than the pump beam radius, it is assumed that the probe overlaps with a region of approximately constant peak irradiance from the pump. After averaging over one thousand probe pulses at each time delay, the change in optical density ($\Delta OD(\lambda, t)$) was recorded as a function of wavelength (λ) and delay time (t). The reflectance change spectra ($\Delta R(\lambda, t)$) of the WLC probe pulses were calculated from measured $\Delta OD(\lambda, t)$ for a variety of peak pump irradiances by $\Delta R(\lambda, t) = R(\lambda) \cdot \left(10^{\Delta OD(\lambda, t)} - 1\right)$, where $R(\lambda)$ is measured linear reflectance spectrum.

3.2.3 Linear optical properties

The design criteria of the **Narrowband NLO Device** is set as follows: a low reflectance ($R(\lambda = 568$ nm, $\Theta = 45°) < 10\%$) at the first incidence angle, a high reflectance ($R(\lambda = 568$ nm, $\Theta = 0°) > 85\%$) at the second incidence angle. Note that this criteria is set with a low linear reflectance (high linear absorptance) at $\Theta = 45°$ for a control pulse, but a high linear reflectance (low linear absorptance) at $\Theta = 0°$ for a signal pulse. Therefore, the

high linear absorptance of a control pulse at $\Theta = 45°$ is capable of driving strong thermal nonlinearities of 23 nm-thick Au in the **Narrowband NLO Device**, and consequently producing a strong reflectance change on the signal pulse.

In contrast, the low linear absorptance at $\Theta = 0°$ reduces self-induced reflectance changes from a signal pulse even with a high peak power. The choice of wavelengths and incidence angles of either control or signal pulses is arbitrary and can be tuned by varying the thickness combination of two ZrO_2 layers simulated through the transfer-matrix method. The same design process simulated by the transfer-matrix method has been explained in details and shown in Figure 9.
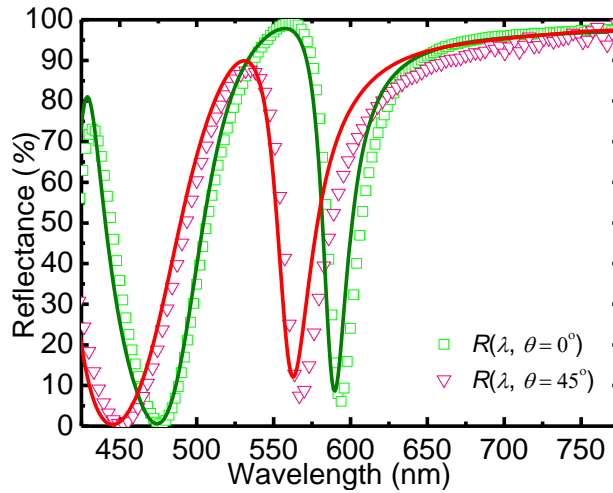
Figure 16: Measured (symbols) and simulated (lines) reflectance spectra at visible wavelengths and two angles of incidence (green, $R(\lambda, \Theta = 0°)$) and (red, $R(\lambda, \Theta = 45°)$) for the sample, Narrowband NLO Device, where the polarization of the incidence light at $\Theta = 45°$ was transverse magnetic (p-pol).

Figure 16 shows a comparison between measured and simulated reflectance spectra of the sample ($R(\lambda, \Theta)$) at visible wavelengths. Simulated reflectance spectra were calculated using the transfer-matrix method. Figure 16 shows a good match between measured (symbols) and simulated reflectance spectra (lines), which simultaneously verifies both the fabrication process and the simulation. In addition, the measured reflectance spectra meet the chosen design criteria by $R(\lambda = 568 \text{ nm}, \Theta = 45°) = 7\%$ and $R(\lambda = 568 \text{ nm}, \Theta = 0°) = 98\%$.

Note that reflectance ($R(\lambda, \Theta)$) and absorptance ($A(\lambda, \Theta)$) spectra of the **Narrowband NLO Device** are complimentary across the visible spectral region as expected from its negligible transmittance. Its component 100 nm-thick Ag layer are thicker than the penetration depth of lights at visible wavelengths. Hence, the **Narrowband NLO Device** has a high angular dependence not only in reflectance but also in absorptance. For example, $A(\lambda=568$ nm, $\Theta=45°) = 93\%$ and $A(\lambda=568$ nm, $\Theta=0°) = 2\%$ are calculated from measured values of $R(\lambda=568$ nm, $\Theta=45°) = 7\%$ and $R(\lambda=568$ nm, $\Theta=0°) = 98\%$.

For **Narrowband NLO Device**, the linear absorptance of a control pulse at $\Theta = 45°$ is maximized by $A(\lambda=568$ nm, $\Theta=45°) = 93\%$, closed to a complete absorption of 100%. This very high linear absorptance of the **Narrowband NLO Device** is primarily attributed to its component 23 nm-thick Au thin film, with negligible absorption in its component 100 nm-thick Ag film, and no absorption in its two ZrO_2 films.

3.2.4 Nonlinear optical properties

The NLO properties of the **Narrowband NLO Device** were characterized by a commercially available white-light (WLC) continuum pump-probe spectroscopy system (HELIOS, ultrafast system). A pump pulse (presenting as a control pulse in Figure 15) was tuned to a wavelength of 568 nm, and a WLC (420 - 950 nm) probe pulse was used to measure reflectance changes spectra $\Delta R(\lambda, t_{peak})$ at $\Theta = 0°$ across the visible spectral region. Measured values of $\Delta R(\lambda, t_{peak})$ of the **Narrowband NLO Device** are shown in Figure 17 and are compared with the **Broadband NLO Device** for $\Delta R(\lambda, t_{peak})$ at the same incidence angle of $\Theta = 0°$. Here, t_{peak} denotes the delay time between a probe and a pump pulse that yields the maximum value of $\Delta R(\lambda, t_{peak})$ in the temporal ranges studied.

The two pump-probe experiments were individually operated at the same **Narrowband NLO Device** sample to characterize its angularly dependent NLO properties by different beam geometries. The first beam geometry (non-collinear beam

geometry) has a pump pulse of wavelength 568 nm at $\Theta = 45°$ and a WLC probe pulse at $\Theta = 0°$. The second beam geometry (collinear beam geometry) has a pump pulse of wavelength 607 nm at $\Theta = 0°$ and a WLC probe pulse at nearly the same angle of incidence. Pump-probe experiments with both beam geometries have been illustrated in Figure 18, and the $\Delta R(\lambda, t)$ values measured across the whole visible spectrum by a WLC probe pulse suggesting control (pump) and signal (probe) pulses in all-optical control applications can have a wide range of combinations between their wavelengths and incidence angles.

Both, the **Narrowband NLO Device** and **Broadband NLO Device** use the same four-layer metal-dielectric thin-film structure (shown in Figure 15):

Narrowband NLO Device: Glass/Ag(100 nm)/ZrO$_2$(389 nm)/Au(23 nm)/ZrO$_2$(133 nm),
Broadband NLO Device: Glass/Ag(100 nm)/SiO$_2$(81 nm)/Au(23 nm)/SiO$_2$(81 nm),

but the dielectric layers and thicknesses have been chosen to allow the structures to present narrow or broad spectral and angular bandwidths and to ease their fabrication. The **Narrowband NLO Device** were firstly designed and fabricated using the same dielectric layers SiO$_2$, and it was found that the required SiO$_2$ thickness is too thick (up to 528 nm) to allow fabrications by the e-beam deposition system used here, causing a delamination of the whole thin-film structure. Hence, a dielectric with high refractive index values (n = 2.2) ZrO$_2$ was used to replace (n = 1.5) SiO$_2$ layers and provide an equivalent optical path length by a thinner layer thickness. Not only the delamination can be avoided, and the linear optical properties of the **Narrowband NLO Device** design are also preserved with a faster e-beam deposition process after reducing the total layer thickness.

48

3.2.5 Pump-probe experiments
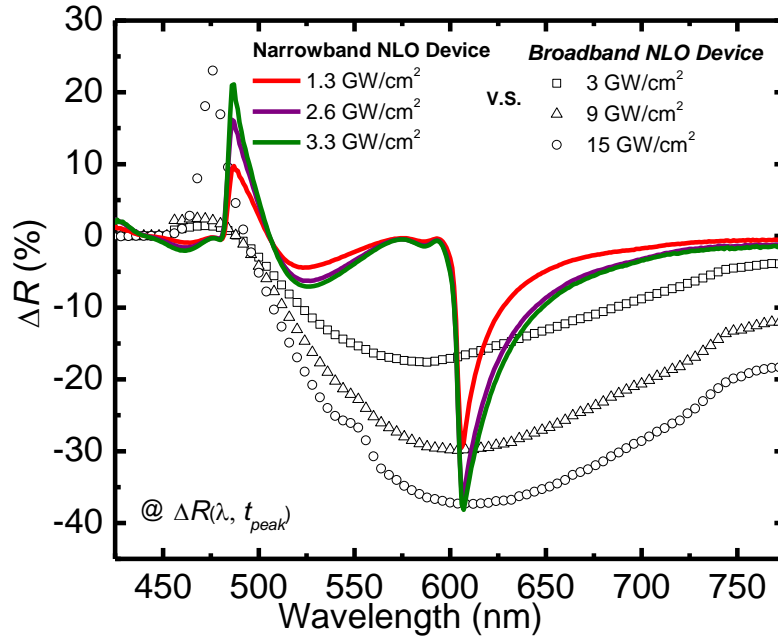
Figure 17: Reflectance changes $\Delta R(\lambda, t_{peak})$ at the $\Theta = 0°$ compared between the Narrowband NLO Device (lines) and Broadband NLO Device (symbols). Narrowband NLO Device is pumped by pump pulses at the wavelength 568 nm and $\Theta = 45°$ with different peak pump irradiance 1.3 (red line), 2.6 (purple line), and 3.3 (green line) GW/cm^2; Broadband NLO Device is pumped by pump pulses at 550 nm and $\Theta = 0°$ with different peak pump irradiances 3 (rectangular), 9 (triangular), 15 (circle) GW/cm^2.

By design, the NLO response of the **Narrowband NLO Device** presents narrow spectral bandwidth characteristics on $\Delta R(\lambda, t_{peak})$, as shown in Figure 17, in contrast to the NLO response of the **Broadband NLO Device**. These two NLO devices illustrate the flexibility that the proposed four-layer metal dielectric structure can present for the design of NLO devices with different optical properties. It is important to note that the **Narrowband NLO Device** requires significantly less peak pump irradiance to produce the same ΔR when compared to the NLO response of the **Broadband NLO Device**. For instance, at $\Delta R(\lambda = 607$ nm, $t_{peak}) = -29\%$, the peak pump irradiances increases from 1.3 GW/cm^2 for the **Narrowband NLO Device** to 9 GW/cm^2 for the **Broadband NLO Device**. Similarly, at $\Delta R(\lambda = 607$ nm, $t_{peak}) = -38\%$, the pump peak irradiances increases

49

from 3.3 to 15 GW/cm^2. Hence, the required peak pump pulse irradiance required to operate the **Narrow NLO Device** is reduced by at least four times compared to those required to operate the **Broadband NLO Device.** This reduction in pump power is clearly attractive for all-optical applications. Finally, it should be noted this difference in driving pump power is a direct result of differences in absorptance values between devices: $A(\lambda = 568$ nm, $\Theta = 45°) = 93\%$ on the **Narrow NLO Device** and $A(\lambda = 550$ nm, $\Theta = 0°) = 55\%$ on the **Broadband NLO Device**.

Here it is worth pointing out that the previous comparison of ΔR values has been made at the wavelength of maximum modulation, which does not correspond to 568 nm for the **Narrowband NLO Device**. Its ΔR values only reach a magnitude of -0.9% at the wavelength of 568 nm, but its maximum ΔR values are at 607 nm with a magnitude of - 38 % excited by the same peak pump irradiance of 3.3 GW/cm^2. Hence, the **Narrowband NLO Device** works best in non-degenerate pump-probe operation. In this particular example, for a pump wavelength of 568 nm wherein $A(\lambda=568$ nm, $\Theta=45°) = 93\%$ and for a probe wavelength of 607 nm wherein $A(\lambda= 607$ nm, $\Theta=0°) = 50\%$. Given the large linear absorption at 607 nm, it is important not only to characterize the NLO response produced by a control pulse at 568 nm incident at $\Theta = 45°$, but also to consider the NLO response induced by a high peak power signal pulse at 607 nm incident at $\Theta = 0°$. Pump-probe experiments with non-collinear and collinear beam geometries were used to characterize both conditions. Figure 18 shows a comparison of the dynamic NLO response measured under these two conditions. The temporal evolution of $\Delta R(\lambda =607$ nm, t) for a non-collinear pump-probe geometry (Figure 18(a)) demonstrates that $\Delta R(\lambda =607$ nm, t) reaches larger values at lower peak irradiances than in the collinear pump-probe geometry (Figure 18(b)). For instance, $\Delta R = $ -29% at 1.3 GW/cm^2 in a non-collinear geometry compared to $\Delta R = $ -32% at 3.7 GW/cm^2 in a collinear geometry. At a pump irradiance of 19 GW/cm^2, Figure 18(b) also shows a distinct temporal evolution of $\Delta R(\lambda =607$ nm, t) with a delayed response reaching a maximum value of around -34%. Similar

dynamic characteristics have been reported in single Au films [18, 48], and have been attributed to a change of the electronic specific heat with increased temperature. It is known that higher pump irradiances result in increasing electron temperatures and greater electronic specific heat, and ends up a longer thermal-relaxation times.
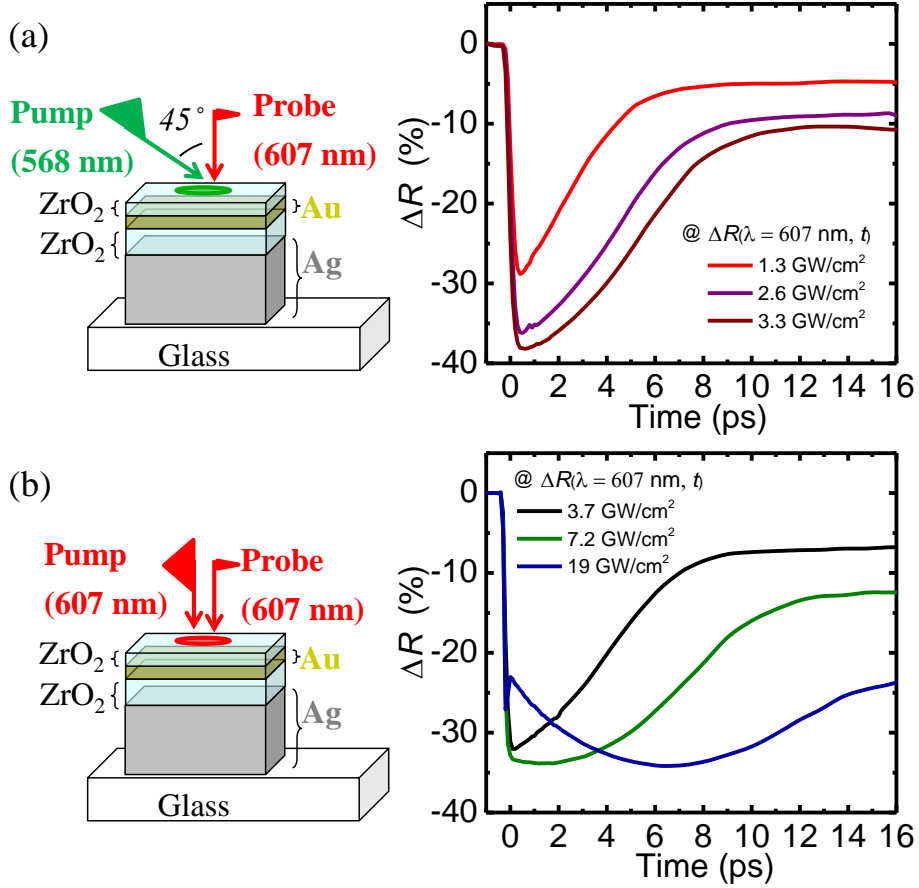
Figure 18: (a) and (b) Temporal dependence of reflectance changes $\Delta R(\lambda = 607$ nm, t) for the Narrowband NLO Device at probe wavelength 607 nm for different peak pump irradiances measured by pump-probe experiments using a non-collinear (Figure 12(a)) and collinear beam geometry (Figure 12(b)) and illustrated in each left figures, respectively.

This result shows the NLO response of the **Narrowband NLO Device** is more sensitive by exciting at $\Theta = 45°$ than at $0°$. To illustrate this better Figure 19 displays the absolute reflectance calculated by $R(\lambda = 607$ nm) $+ \Delta R(\lambda = 607$ nm, $t_{peak})$, where $R(\lambda = 607$ nm) is the measured linear reflectance at the normal incidence shown in Figure 16.

51
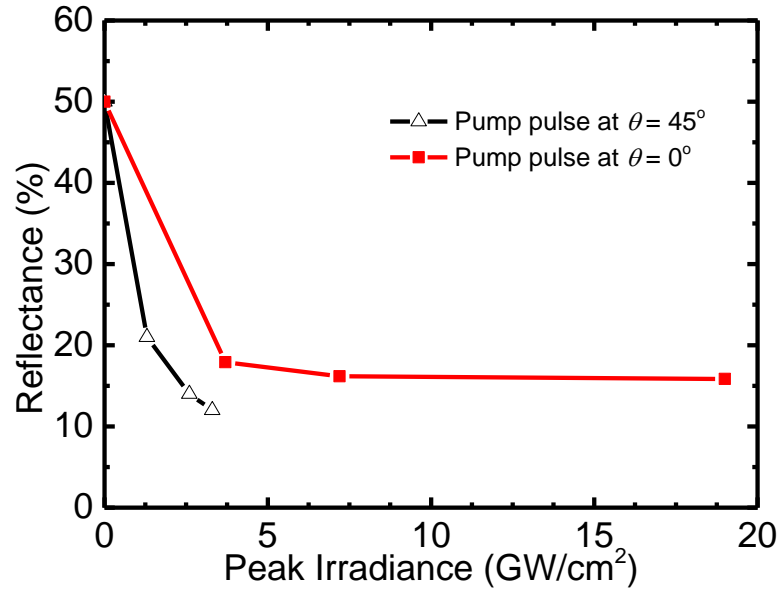
Figure 19: Irradiance dependent reflectance (%) at the wavelength 607 nm by adding linear reflectance $R(\lambda = 607$ nm$)$ with measured $\Delta R(\lambda = 607$ nm, $t_{peak})$ compared between pumping at $\Theta = 45°$ (black line and symbol) and $\Theta = 0°$ (red line and symbol) with beam geometries as shown in Figure12(a) and (b), respectively.

In summary, the **Narrowband NLO Device** presents a high angular dependence in its linear and NLO properties. The customized angular dependence can simultaneously enhance the NLO response excited by the control pulse and reduce the self-induced NLO responses from high peak-power signal pulse. The extremely large magnitude of ΔR, ultrafast response, and adjustable angular and spectral bandwidth are attractive for NLO devices to all-optically control for high peak power signal pulses with different engineering requirements.

3.3 Conclusion

This chapter presented studies of noble-metal nonlinear optical (NLO) device structures which can amplify the strong and ultrafast NLO properties of an Au thin film at visible wavelengths. Spectral and angular bandwidths of the NLO device are adjustable while maintaining a large nonlinear reflectance change. The same four layer thin-film structure

can be tuned to present broad or narrow spectral and angular bandwidths. The linear optical properties of these NLO devices can therefore be tuned without compromising their NLO properties, and can be of great interest for a wide variety of all-optical applications in the visible spectral range.

The **Narrowband NLO Device** not only reduces the peak power consumption of a control pulse used in exciting ultrafast reflectance changes, but opens up a new design of all-optical controls for high peak-power signal pulses. This attractive optical device (**Narrowband NLO Device**) will be further integrated and developed into a novel dose-control system (**ultrafast all-optical shutter**) for medical and laser manufacturing applications present in the next chapter.

One part of results in CHAPTER 3 has been published in the journal Optics Express: J. Hsu, C. Fuentes-Hernandez, A. R. Ernst, and B. Kippelen, "Ultrafast nonlinear mirrors with broad spectral and angular bandwidths in the visible spectral range." The other part of results is being prepared in a paper draft "Angular sensitivity of nonlinear optical dual metal-layer device for all-optical control of high intensity signal pulse". A provisional patent covering the devices described in this chapter: "Nonlinear optical devices for ultrafast optical applications," (GTRC ID 6221) has been filed to the Georgia Tech office of Technology Licensing.

CHAPTER 4: ULTRAFAST ALL-OPTICAL SHUTTER FOR MEDICAL AND LASER MANUFACTURING APPLICATIONS

To date, reports of ultrafast optical shutters in the literature are scarce [71-73]. The performance of these shutters is limited in their spectral range of operation; none of them offer the ability to easily adjust the shutter opening window (i.e. actively control the time during which the shutter remains open) nor the ability to modulate high peak-power optical pulses [71-73]. Accordingly, there is a need to study **ultrafast all-optical shutter** to generate high peak-power sub-nanosecond pulses with adjustable temporal pulse widths.

4.1 General timing mechanism and setup
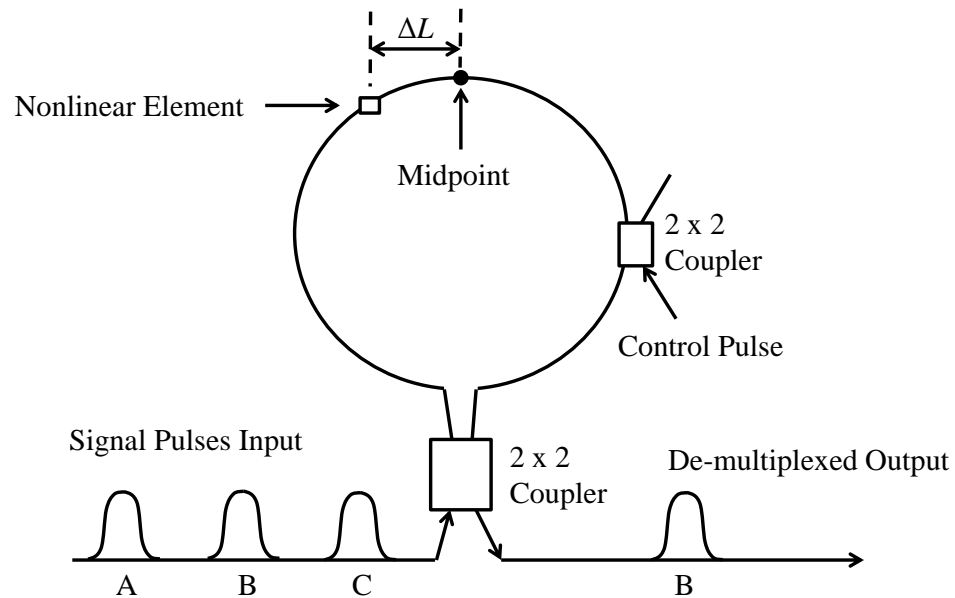
Figure 20: The general configuration of the terahertz optical asymmetric de-multiplexer (TOAD).

The present **ultrafast all-optical shutter** adopts a timing mechanism derived from the terahertz optical asymmetric demultiplexer (TOAD) introduced by Sokoloff, et al. [74]. Figure 20 shows the TOAD configuration comprising a fiber loop with a first 2 x 2

54

coupler. The first coupler is used for introducing a series of signal pulses. On the other hand, the second intra-loop 2 x 2 coupler is used for introducing a control pulse to optically pump a nonlinear optical element. The position of the nonlinear optical element is offset from the midpoint of the loop by a distance (ΔL) defined as an optical path length. The TOAD architecture uses the off-center position of the nonlinear optical element to determine an adjustable sampling window (Δt). The duration of Δt can be further calculated by the following equation:

$$\Delta t = \frac{2\Delta L}{c} \quad \text{and} \quad \tau_{rise} < \Delta t \ll \tau_{fall} \tag{4-2}$$

where c is the speed of light, τ_{rise} is the turn-on time of the nonlinearity of the nonlinear optical element, and τ_{fall} is the relaxation time of the nonlinearity. The pre-set Δt determines which of the signal pulses would be affected and let through the output port. Figure 20 illustrates that three signal pulses enter at the input port: A, B, and C. The de-multiplexer lets the pulse B pass only based on the adjustable sampling window (Δt). The full operation process of TOAD has been described in detail in the reference [74].

The ideal behind the proposed work is to use a similar timing mechanism as used in TOAD, adopts it for the desired function of the **ultrafast all-optical shutter** as shown in Figure 28(b), and will later explain in the proposed **ultrafast all-optical shutter** in detail. The timing mechanism is formulated in Eq. 4-2 and shows that an adjustable sampling window Δt can be set by choosing ΔL. For instance, the offset introduced by inserting a 0.5 mm-thick glass slab with a refractive index value of 1.5 results in an adjustable sampling window of $\Delta t = 2 \cdot (0.5 \text{ mm} \cdot 1.5)/c = 6 \text{ ps}$.

Other timing configurations could also be used to define an adjustable sampling window (Δt) in the **ultrafast all-optical shutter,** such as colliding-pulse Mach-Zehnder (CPMZ) and symmetric Mach-Zehnder (SMZ) [75, 76]. All these architectures have been

developed as all-optical interferometric switches, mainly, for high bandwidth de-multiplexing in telecommunication signals. Otherwise, these architectures have not been exploited for all-optical control at visible wavelengths due to the limited number of materials having a large nonlinear optical response in the visible spectral region.
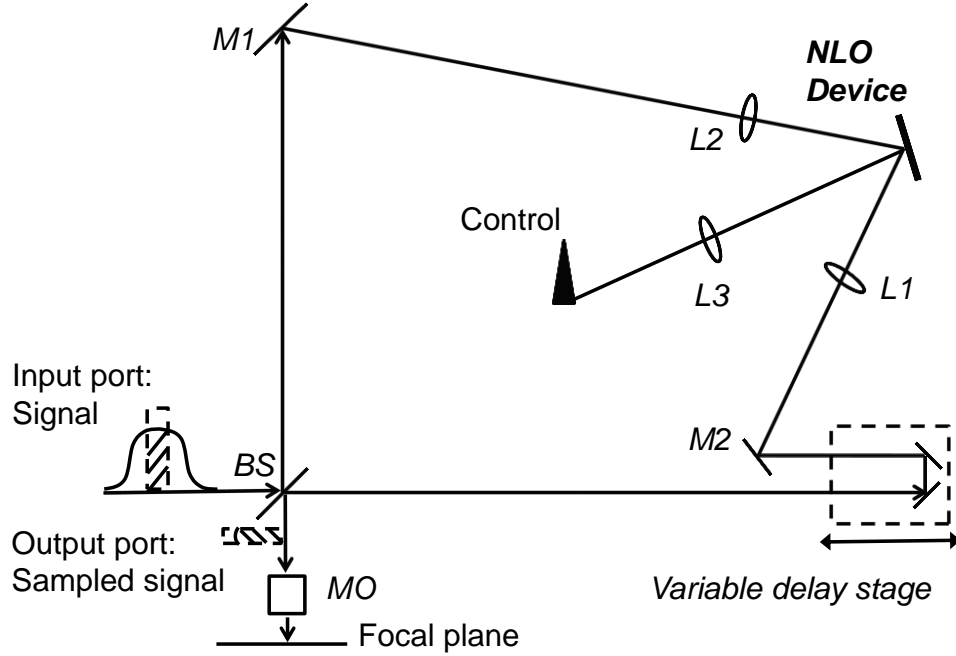
Figure 21: Experimental setup of an ultrafast all-optical shutter, where *BS* is the non-polarized beam splitters, *M1* and *M2* are silver mirrors, the *NLO Device* is a nonlinear optical device (Narrowband NLO Device described in Section 3.2), *L1*, *L2*, and *L3* are lenses and *variable delay stage* is an optical delay line; A signal pulse incident from the input port and a control pulse injects on the Narrowband NLO Device at normal incidence. The temporally sampled signal pulse transmits to the output port, and then is focused by a microscope objective (MO) down to the focal plane and causes non-thermal ablations.

Figure 21 shows an experimental setup of the **ultrafast all-optical shutter**, where the nonlinear optical element is a **Narrowband NLO Device**, the nonlinear optical device discussed in the Section 3.2. An optical delay line (variable delay stage shown in Figure 21) consisting of a translation stage with a retro-reflector is used to define ΔL, and consequently Δt. The resolution of the ΔL, and consequently of Δt, can be can be precisely controlled down to a few tens of micrometers. Hence, Δt is easily, and very accurately adjustable by varying the value of ΔL with a resolution up to hundreds of

femtoseconds. The limitation to the minimum and maximum value of Δt that can be used, as shown in Eq. 4-2, is the temporal response of the nonlinear optical element used. Pump-probe experiments presented in Section 3.2.5 show that the **Narrowband NLO Device** displays transient reflectance changes (ΔR) with rising times on the order of $\tau_{rise} \sim 500\, fs$ and relaxation time in the rage of $\tau_{fall} > 80\, ps$, when optically pumped by a $60\, fs$ half-width-1/e (HW 1/e) pulse with a peak irradiance 19 GW/cm^2 (see Figure 18). Hence, it is expected that the **ultrafast all-optical shutter** will be broadly tunable with adjustable sampling windows from picosecond to femtosecond response times ($500\, fs < \Delta t < \tau_{fall}$ where $\tau_{fall} > 80\, ps$).

The **ultrafast all-optical shutter** has an optical layout comprised of: a 50:50 non-polarized beam splitter (*BS*); two silver mirrors: *M1* and *M2*; three lenses: *L1* to *L3*; a nonlinear optical (NLO) device: **Narrowband NLO Device**; and a linear optical element consisting of an optical delay line (variable delay stage) consisting of a translation stage with a retro-reflector.

An optical loop (ring interferometer) is formed for a signal pulse through the use of a 50:50 non-polarized beam splitter (*BS*), two silver mirrors: *M1* and *M2*, one nonlinear optical device: the **Narrowband NLO Device**, and an optical delay line: *variable delay stage* to introduce the adjustable sampling window of Δt. The variable delay stage offsets the **Narrowband NLO Device** from the midpoint of the loop by ΔL. A signal pulse incident from the input port enters the loop and is firstly split into two pulses by the *BS* to create a clockwise propagating pulse and a counter-clockwise propagating pulse. For example, consider a clockwise propagating pulse: it reflects from *BS* into *M1,* and then focuses through *L2* on the **Narrowband NLO Device**. The clockwise propagating pulse subsequently reflects off the **Narrowband NLO Device**, is then converted back to a collimated pulse by *L1*, reflects off M2, and transmits through a *variable delay stage.* Finally, the pulse transmits through *BS*, and returns to the input port.

Both clockwise and counter-clockwise propagating pulses experience exactly the same loop path only in a reversed direction. Hence, both signal pulses temporally overlap with each other at the output port. A lossless beam splitter gives a phase shift of $\emptyset_t - \emptyset_r = 90°$ [77, 78], where $\emptyset_t$ and $\emptyset_r$ are phases of transmitted and reflected light beams. In terms of the output port, two split signal pulses return and experience a $2\emptyset_r + \emptyset_{loop}$ and $2\emptyset_t + \emptyset_{loop}$ phase shift in clockwise and counter-clockwise direction, respectively, where $\emptyset_{loop}$ is the arbitrary phase shift given by the loop. The relative phase shift between recombined pulses is therefore $2\emptyset_t - 2\emptyset_r = 180°$ and causes a completely destructive interference. Therefore, no signal pulse is allowed to transmit to the output port until the control pulse is present. In other words, the **ultrafast all-optical shutter** is closed by default. At the input port, both split signal pulses return with the same phase shift of $\emptyset_t + \emptyset_r + \emptyset_{loop}$, and make a completely constructive interference. The energy conservation law makes any incidence light at the input port be totally reflected, since the output port is closed by default. This type of loop was called a conventional "loop mirror" [79].
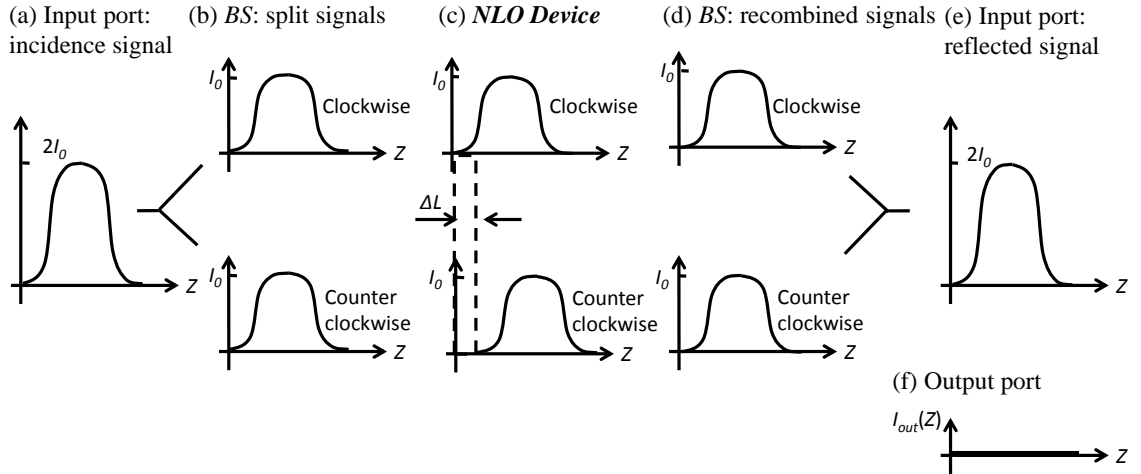
Figure 22: The propagation analysis of the signal pulse with a spatially dependent irradiance profile ($I(Z)$) of (a) the incidence signal at the input port, (b) two split signals (clockwise and counter-clockwise propagating pulses) at the *BS*, (c) two split signals at the nonlinear optical device, (d) two recombined signals back to the *BS*, (e) the reflected signal at the input port, and (f) the signal at the output port, where Z is the local position, *ΔL* defines the adjustable sampling window *Δt*, and $2I_0$ and I_0 are the peak irradiance of the incidence signal before and after split, respectively.

58

Figure 22(a) to 22(f) subsequently shows the propagation analysis of the above process by a spatially dependent irradiance profile ($I(Z)$). Figure 22(a) initially shows the irradiance profile of the incidence signal pulse at a peak irradiance $2I_0$ assuming a Gaussian profile. The *BS* then splits the incidence signal pulse into a clockwise and a counter-clockwise propagating pulse of equal peak irradiance I_0 and their irradiance profiles are overlapped as shown in Figure 22(b). Figure 22(c) shows that there is a temporal offset of Δt between two split signal pulses at the **Narrowband NLO Device**, because the clockwise propagating pulse travels an extra distance of ΔL introduced by the optical delay line compared to the counter-clockwise propagating pulse, as shown in Figure 21. This Δt results in the clockwise propagating pulse arriving at the **Narrowband NLO Device** after the counter-clockwise propagating pulse. However, Figure 22(d) shows that the irradiance profile of two split signal pulses temporally overlap after the two pulses travel the whole loop in a reversed direction and recombine at the *BS* as shown in Figure 21. Both clockwise and counter-clockwise propagating pulses pass through the optical delay line once. Finally, Figure 22(e) shows completely constructive interference of two recombined signal pulses at the input port and Figure 22(f) shows a completely destructive interference at the output port.
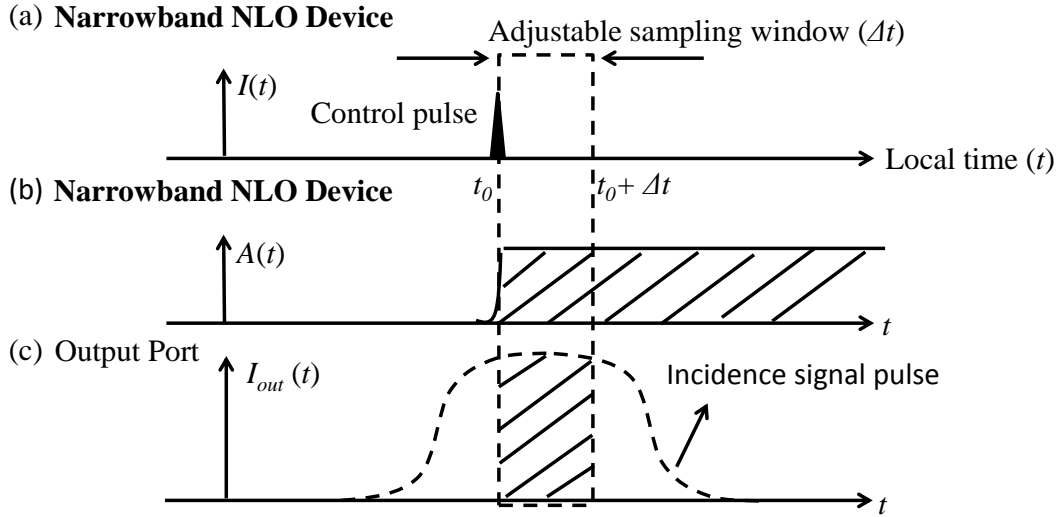
Figure 23: The temporal analysis of (a) irradiance profile ($I(t)$) of the control pulse, (b) the complex amplitude modulation ($A(t)$) for the transient reflectance coefficient of the Narrowband NLO Device, and (c) the irradiance profile ($I_{out}(t)$) of the signal pulse sampled at the output port. The shaded area represents the sampled portion which has experienced $A(t)$. The local time (t) is with respect to the position.

When a control pulse is introduced in the setup, as shown in Figure 21, it excites the **Narrowband NLO Device** at the time point t_0 as shown in Figure 23(a). This excitation induces a strong transient reflectance coefficient change (including amplitude and phase modulations) which are symbolized in a temporally dependent function of complex amplitude ($A(t)$), shown in Figure 23(b) and shaded. The nonlinear optical response of the **Narrowband NLO Device** presents a fast rising time and a slow relaxation time upon being illuminated by a control optical pulse. For instance, a 60 fs control pulse should present a fast rising time less than 500 fs and a slow relaxation time about several tens of ps. The preliminary experiments of the **ultrafast all-optical shutter** using a 60 fs control pulse will be later introduced in details.

The local time (t) of Figure 23 is with respect to the position. Figure 23(c) shows the irradiance profile ($I_{out}(t)$) at the output port. The **ultrafast all-optical shutter** therefore opens during the adjustable sampling window (Δt) and closes outside the window. The detailed temporal analysis will be discussed later. During this period the

ultrafast all-optical shutter remains open, leading to an output irradiance profile of $I_{out}(t)$, shown in Figure 23(c) (filled area). The peak output irradiance of $I_{out}(t)$ can be calculated by following a basic interferometric equation [76]:

$$\frac{I_{out}}{I_{in}} = \frac{1}{4}\left\{ R_1 + R_2 - 2\sqrt{R_1 R_2}\cos(\phi_1 - \phi_2) \right\} \tag{4-3}$$

where the input signal pulse has the peak input irradiance of I_{in}, the output signal pulse has the peak output irradiance of I_{out}, the transient reflectance ($R_{1,2}$) and transient phase shift ($Ø_{1,2}$) when signal pulses transverse the **Narrowband NLO Device**, and subscripts 1 and 2 denote a clockwise and counter-clockwise propagating signal pulse, respectively. Therefore, in the absence of a control optical pulse, the relative phase shift between said first and second signal optical pulses is $Ø_1 - Ø_2 = 2Ø_t - 2Ø_r = 180°$, causing a complete destructive interference at the output port of the ring interferometer. In the absence of a control optical pulse, the ultrafast all-optical shutter is closed by default.
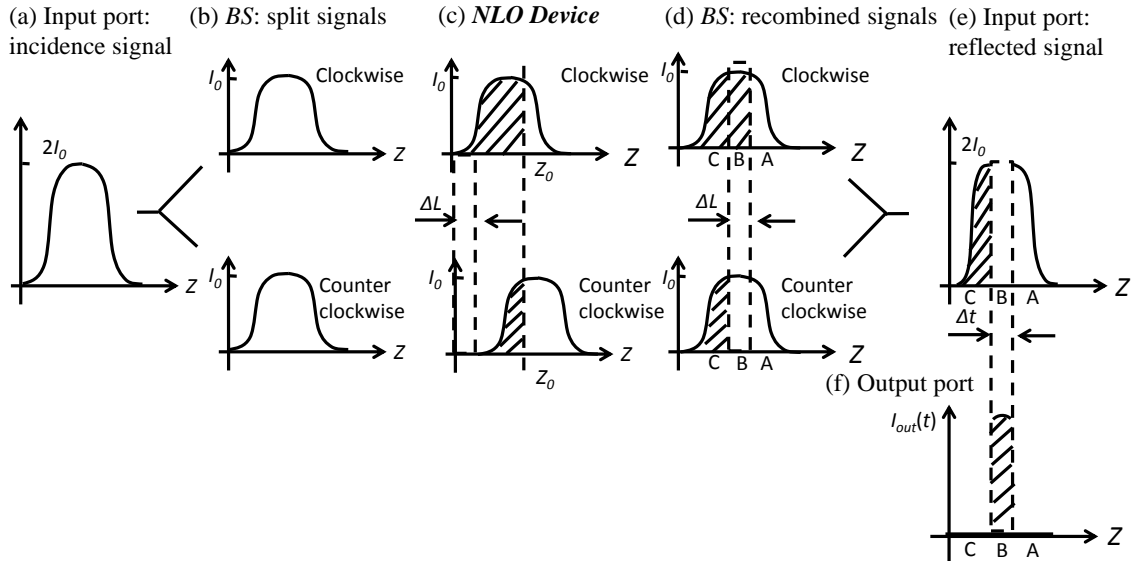
Figure 24: The propagation analysis of the signal pulse with a spatially dependent irradiance profile ($I(Z)$) of (a) the incidence signal at the input port, (b) two split signals (clockwise and counter-clockwise propagating pulses) at the *BS*, (c) two split signals at the nonlinear optical device, (d) two recombined signals back to the *BS*, (e) the reflected signal at the input port, and (f) the sampled signal pulse at the output port, where *Z* is the local position, *ΔL* defines the adjustable sampling

window of *Δt*, and **2I₀** and **I₀** are peak irradiances of the incidence signal before and after split, respectively.

In the following part, the propagation analysis when the control pulse is introduced will be explained in detail. The propagation evolution with a control pulse follows exactly that of the case without the control pulse, as shown in Figure 22. However, the **Narrowband NLO Device** is now excited by the control pulse at the position Z_0 and causes nonlinear modulations defined by $A(t)$ as shown in Figure 23(b). Hereafter, the portion of the signal pulse which experiences $A(t)$ will be shaded, as shown in Figure 24. The clockwise propagating pulse arrives at the **Narrowband NLO Device** behind the counter-clockwise propagating pulse as shown in Figure 24(c). Consequently the clockwise propagating pulse experiences a longer period of modulations, defined by Δt, than the counter-clockwise propagating pulse as shown in Figure 24(c). Figure 24(d) shows that at the output port, the irradiance profiles of these signal pulses overlap, as initially shown in Figure 24(b); since the two pulses travel the same loop path just in a reversed direction and recombine at the *BS* as shown in Figure 21.

For illustration convenience, Figure 24(d) shows that both recombined signal pulses are decomposed into three subsequent parts: A, B, and C. Figure 24(d) shows both recombined signal pulses are symmetrically un-modulated for the part A and symmetrically modulated for the part C. This leads to a completely destructive interference both in the part A and C which results in zero irradiance at the output port. Hence, the **ultrafast all-optical shutter** closes in the part A and part C with no signal pulses transmitted. Finally, Figure 24(d) shows only the part B of the recombined signal pulses, which is anti-symmetrically modulated. It is modulated for the clockwise propagating pulse but un-modulated for the counter-clockwise propagating pulse. The part B of recombined signal pulse at the output port undergoes a constructive interference, thus producing an output. Therefore, Figure 24(f) shows that the **ultrafast all-optical**

shutter opens only in the part B. The duration of the part B matches with the adjustable sampling window Δt.

4.2 Temporal-scan experiments

The **ultrafast all-optical shutter** is designed to provide an ultrafast timing mechanism, with opening and closing times on the order of several hundreds of fs to ps, the adjustable opening window (adjustable sampling window as shown in Figure 23) is easily pre-set and adjusted by varying the optical delay within the ring interferometer

In this section, the dynamic of the **ultrafast all-optical shutter** will be characterized, and be described as an impulse response of an optical system. Here, a temporal-scan experiment is set up as shown in Figure 25. The experiment is set to measure the impulse response of the **ultrafast all-optical shutter**. However, the impulse response can be widely used not only in simulating the sampling process, but also calculating a temporal response of shutter output with response to any control pulse with an arbitrary temporal profile by a convolution between the control pulse profile and the impulse response.

The impulse response as a function of time will be scanned in a time-resolved experiment as a proof-of-principle of the **ultrafast all-optical shutter** to show the temporal profile of its adjustable opening window. Ultrafast applications enable by this **ultrafast all-optical shutter** such as ultrafast photography, time-gated spectroscopy, and photo-electric effects with temporally shaped pulses, which will be further discussed in CHAPTER 5.
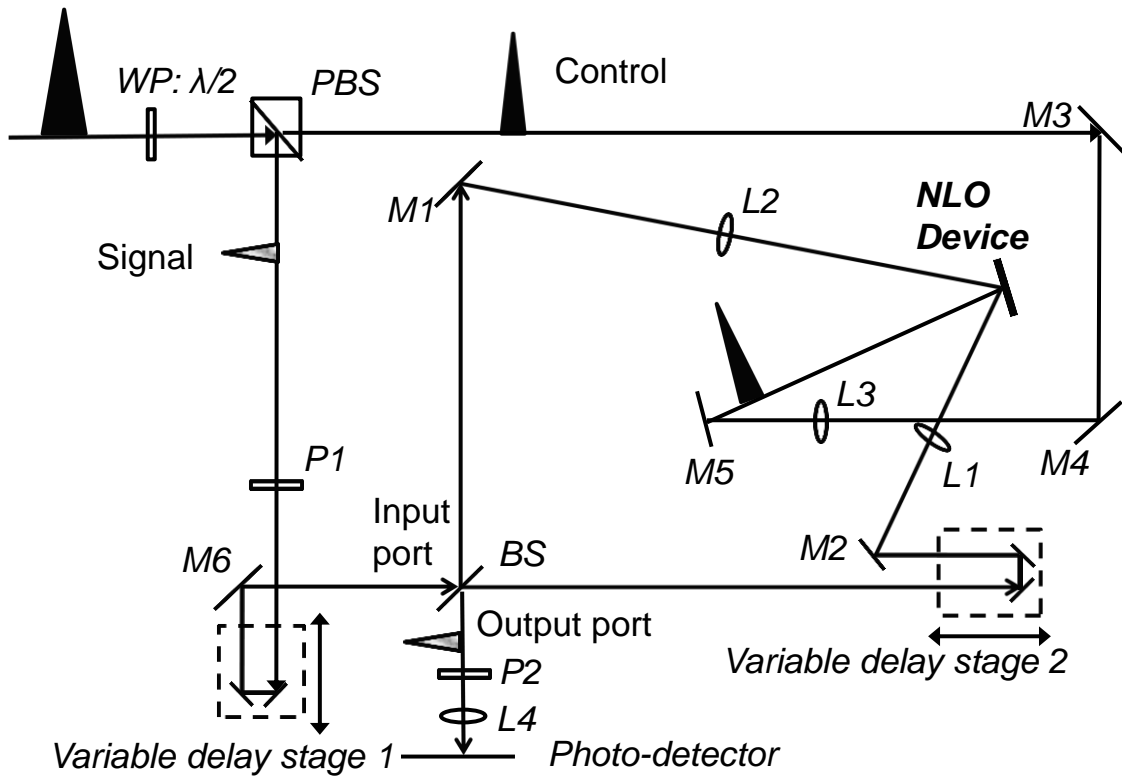
Figure 25: Temporal-scan experiment of an ultrafast all-optical shutter to temporally scan its impulse response and measure the temporal profile of its adjustable opening window, where *BS* and *PBS* are the non-polarized and polarized beam splitters, respectively, *WP* is the half-wave plate, *P1* and *P2* are polarizers, *M1* to *M6* are silver mirrors, the *NLO Device* is a nonlinear optical device (Narrowband NLO Device described in Section 3.2), *L1* to *L4* are lenses, and *Variable delay stage 1* and *Variable delay stage 2* are optical delay lines; A femtosecond laser pulse is split into a high peak-irradiance control pulse and a low peak-irradiance signal pulse, where the control pulse injects on the *NLO Device* at normal incidence, the signal pulse incident from the input port, transmits to the output port, and then is focused down to the *Photo-detector*.

The temporal-scan experiment uses a femtosecond laser system, where its femtosecond laser pulse is obtained from an optical parametric amplifier (OperASolo, Coherent). A seed laser beam from a Ti:Sapphire regenerative amplifier (Libra, Coherent) operating at the wavelength of 800 nm generates a femtosecond pulse through the OperASolo, and the wavelength of the femtosecond pulse can be tuned within the visible spectra range. The femtosecond pulse has a temporal pulse width of 100 fs half-width-1/e (HW 1/e).

Figure 25 shows that the temporal-scan experiment of the **ultrafast all-optical shutter** has an optical layout comprised of: polarized and 50:50 non-polarized beam splitter: *PBS* and *BS*; five silver mirrors: *M1* to *M6*; four lenses: *L1* to *L4*; a nonlinear

64

optical (NLO) device: **Narrowband NLO Device**; and two optical delay line: *Variable delay stage1* and *Variable delay stage 2*, consisting of a translation stage with a retro-reflector, where *Variable delay stage1* and *Variable delay stage2* uses a computer-controlled motorized translation stage and non-motorized translation stage, respectively.

In this configuration, a single femtosecond laser pulse at the wavelength of 594 nm is split into a strong control pulse and a weak signal pulse with a peak irradiance of 123 and 0.35 GW/cm^2 measured at the position of the **Narrowband NLO Device**, respectively, after passing through *WP* and *PBS*. The polarization angle of *WP* is adjusted to maximize the peak irradiance of a control pulse, leading to optimize the excitation of the **Narrowband NLO Device** at the normal incidence, and consequently optimize the operation of the **ultrafast all-optical shutter**. The control pulse was tuned to a spot size of 190 μm (HW 1/e) at the position of the **Narrowband NLO Device**, measured using a knife-edge scan. The signal pulse had a spot size of 100 μm (HW 1/e) at the same position.

The signal pulse passes through the *Variable delay stage1*, which introduces a variable optical path difference between the signal and control pulse, resulting in a time delay between two pulses. This *Variable delay stage1* is gradually scaned through a series of offset positions, and the time-averaged output intensity I(t) of the **ultrafast all-optical shutter** recorded as a function of delay time (t) after averaging over one thousand signal pulses injecting from the input port of the **ultrafast all-optical shutter** and passing through the output port to the *Photo-detector*. Note that time-averaged output intensity I(*t*) can be sensitive to the jitter of laser intensity during acquisition time, so I(t) is calculated from measured time average output $I_{out}(t)$ by $I_{out}(t)/ I_{ref}(t)$ to discriminate signal from noises originated from laser jitters itself, where $I_{ref}(t)$ is measured time-averaged reference intensity sampled out of the same optical setup.

The resolution of the motorized translation stage of *Variable delay stage1*, can be accurately controlled down to a few tens of micrometers. Hence, the time-resolved study from this temporal-scan experiment can therefore be up to a few hundreds of femtoseconds. In addition, Figure 25 also shows that a signal pulse passing through the input and output port of a ring interferometer, where the propagation analysis has been explained in details in Figure 21. In brief, a first and a second split signal optical pulse after *BS* impinge upon the **Narrowband NLO Device** at $\pm 45°$, while the control optical pulse impinges on it at normal incidence. The **Narrowband NLO Device** is designed to present a high linear reflectance at $\pm 45°$ and a low linear reflectance (high linear absorptance) at normal incidence. The high linear absorptance of the control pulse drives the strong thermal nonlinearity of the **Narrowband NLO Device** and produces a strong change of the reflectance at $\pm 45°$.

The second optical delay line: *variable delay stage 2* introduces the adjustable opening window of Δt for the **ultrafast all-optical shutter**. When the *variable delay stage 2* offsets the **Narrowband NLO Device** from the midpoint of the loop (ring interferometer) by ΔL, the adjustable opening window can consequently be preset by Δt. Although the general timing mechanism of the **ultrafast all-optical shutter** has been shown in the last section, the temporal-scan experiment here is used to scan the temporal profile of this adjustable opening window. Note that two polarizers *P1* and *P2* are added into the optical layout shown in Figure 25, because it is found that varying the combination of polarization angles of *P1* and *P2* can further increase the signal-to-noise ratio measured by time-averaged output intensity I(t) of the **ultrafast all-optical shutter**.
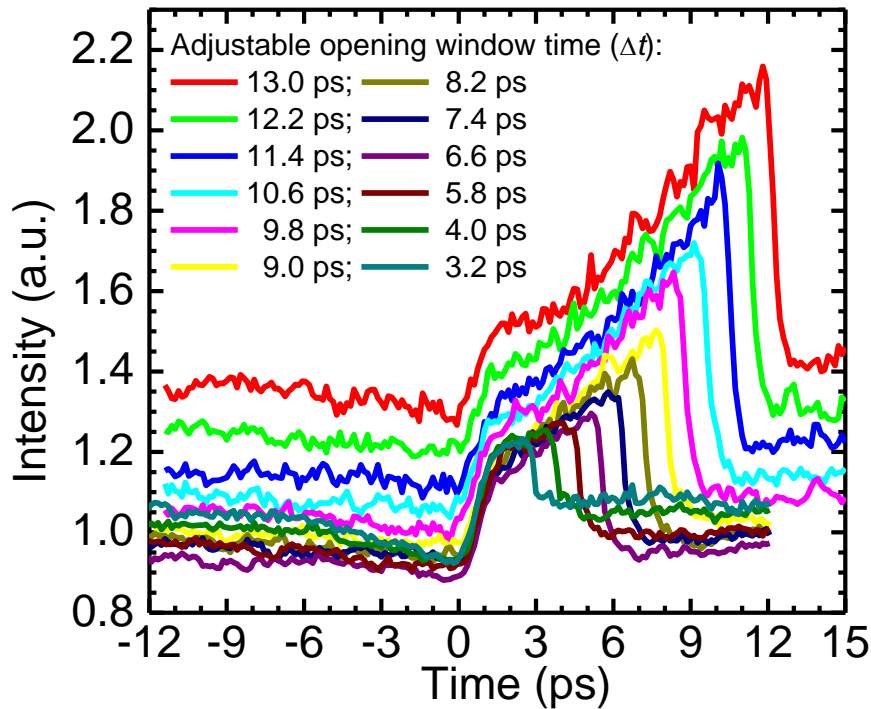
Figure 26: Time-averaged output intensity I(t) of the ultrafast all-optical shutter versus time delay of the signal pulses with respect to the control pulses. This temporal-scan experiment measures a profile of the adjustable opening window opened by the control pulse between the input and output of the shutter. The figure shows 12 different settings of adjustable opening window (Δt) decreasing from 13 ps to 3.2 ps with a constant interval of 0.8 ps.

Figure 26 shows the impulse response of the **ultrafast all-optical shutter** by measuring time-averaged output intensity I(t) with different time delays between a signal and control pulse. The shutter is opened between its input and output port by a femtosecond control pulse, and has a larger value of I(t) within the preset adjustable opening window compared to outside the opening window. The temporal-scan experiment scans the temporal shape of 12 different settings of adjustable opening windows varying from Δt = 13 ps to 3.2 ps with a constant interval of 0.8 ps as shown in Figure 26. The results show that all adjustable opening windows display a consistent temporal shape with a sharp rising edge and a sharp falling edge, both below 1 ps. The preset adjustable opening windows of Δt matches faithfully with the measured values as shown in Figure 26. The adjustable window time is easily set, and is accurately controlled by the *variable delay*

stage 2 as shown in Figure 25, though the optical alignment of the optical delay line can still be further refined to keep values of I(t) be constant when the shutter closes.

It is interesting to note that values of I(t) changes exponentially, which is expected from the exponential decay of thermal nonlinearities of **Narrowband NLO Device** excited by a femtosecond laser pulse as shown in Figure 18. In addition, the shape of opening time window should be tunable, for example, a flat-hat shape can be achieved through a slowly decayed relaxation of thermal nonlinearities either from saturated nonlinearities excited by a very high peak-irradiance control pulse as mentioned in CHAPTER 3, or nonlinearities excited by a temporally shaped nanosecond control pulse with a fast rising time and a slow decay time.

4.3 Potential applications in medical and laser manufacturing

A present challenge in laser manufactures and pulsed-laser surgeries is to achieve precisely all-optical control over high peak power signal pulses. In conventional all-optical control systems, a low intensity signal pulse is modulated in amplitude and/or phase by a high intensity control pulse through the NLO effects excited by the control pulse alone. On the other hand, the all-optical control of non-thermal ablation applications require a high peak-power signal pulse since it needs to have enough energy and power to ablate the targeted materials including tissues. To achieve such properties the linear and NLO properties need to be precisely engineered, so that the nonlinearity can be selectively driven by the control pulse even if the signal pulse also has a high peak power. The **Narrowband NLO Device**, with its extremely large and ultrafast NLO response, offers such unique all-optical control of intense pulses in the visible spectral range and is ideal to develop the proposed novel **ultrafast all-optical shutter** design.

The **ultrafast all-optical shutter** is present to sample a high peak-power nanosecond optical pulse with a wavelength in the visible spectral regions to produce a high peak-power picosecond or femtosecond optical pulse of the same wavelength. The

potential impact of the shutter can enable high-repetition rate and low-cost nanosecond pulse laser systems to be used to produce femtosecond or picosecond laser pulses with properties that are well suited for the non-thermal ablation of materials.

Since the proposed objective of the **ultrafast all-optical shutter** is to sample sub-nanosecond laser pulses from nanosecond laser pulses, the whole optical system should be integrated under a single nanosecond laser system to reduce capital costs. In this complete optical layout, the fast rising edge of a ns control optical pulse needs to be generated by passing a ns laser pulse through a slow saturable absorber, for example, an organic dye DODCI (3,3'-diethyloxadicarbocyanine iodide) [80]. The temporal shape of this ns control pulse can therefore match to excite the preferred temporal response of **Narrowband NLO Device** as shown in Figure 23(b).
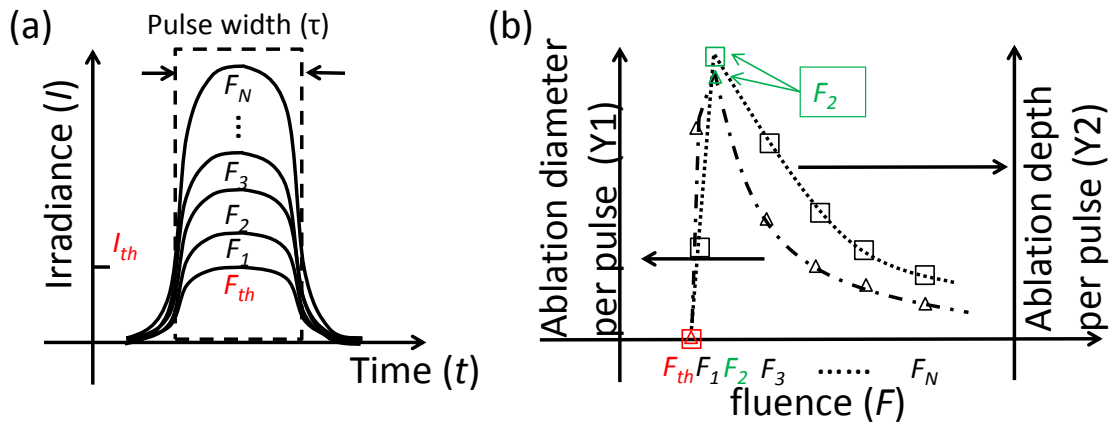
Figure 27: (a) and (b), a femtosecond pulsed-laser surgery study between (a) temporally dependent irradiance profiles ($I(t)$) of a single Gaussian pulse with different fluences per pulse (F) and (b) ablation diameter (Y1 axis on left and labeled by triangular symbols) and depth (Y2 axis on right and labeled in rectangular symbols) per pulse with different F.

The experimental study of femtosecond pulse surgeries on collagen gels and porcine corneas by Kruger and Oraevsky *et al.* [49, 52] reports that both vertical and horizontal precision of the ablated area can be improved, as well as control over cut diameters, depths, and volume removal rates, by selecting the right amount of laser

fluence per pulse (F). Figure 27(a) shows the temporally dependent irradiance profiles ($I(t)$) in a series of pulse fluence per pulse $F = F_{th}$, F_1, F_2, F_3 ... F_N. Each pulse profile of $I(t)$ was experimentally confirmed to be close to a Gaussian pulse with similar temporal pulse width (τ). These pulses can be described as below.

$$I(t) = I_{peak} \exp(-(\frac{t - t_{peak}}{\tau})^2),$$

$$F = \int_{-\infty}^{\infty} I(t)dt = \int_{-\infty}^{\infty} I_{peak} \exp(-\frac{t - t_{peak}}{\tau})^2 dt = I_{peak}\left(\tau\sqrt{\pi}\right),$$

(4-1)

where I_{peak} is the peak irradiance, t_{peak} is the time at which I_{peak} is achieved. Equation 4-1shows a relationship between F and I_{peak} for any Gaussian pulse, and one set of F_{th} and I_{th} is labeled in Figure 27(a).

Figure 27(b) shows a relationship between the ablation diameter (Y1 axis on left) and depth (Y2 axis on right) per pulse for a set of pulses of varying fluences shown in Figure 27(a) as reported by Oraveskey, et al. [52]. The ablation diameter and depth per pulse represent averages from measurements of multiple pulses, as illustrated in Figure 28(a), and will be explained later. Figure 27(b) shows there is a minimum fluence (F_{th}) for a single pulse to reach observable ablation. F_{th} or I_{th} is therefore the damage threshold for ablation and can be determined experimentally. The damage threshold of femtosecond pulsed ablation originates in the optical breakdown mechanism called multi-photon ionization. When simultaneous absorption of multi-photon occurs, they ionize seed electrons and then initiate a chain of ionization, also known as avalanche ionization. Since it requires a minimum number of photons to be simultaneously absorbed (six photons in case of tissues irradiated at the wavelength of 1053 nm), the correspondent damage threshold can be defined in F_{th} or I_{th}. In addition, Figure 27(b) also shows that

both an ablation diameter and depth per pulse achieves a maximum point at a fluence per pulse of F_2; resulting in a maximum volume removal rate for ablation by a single pulse.
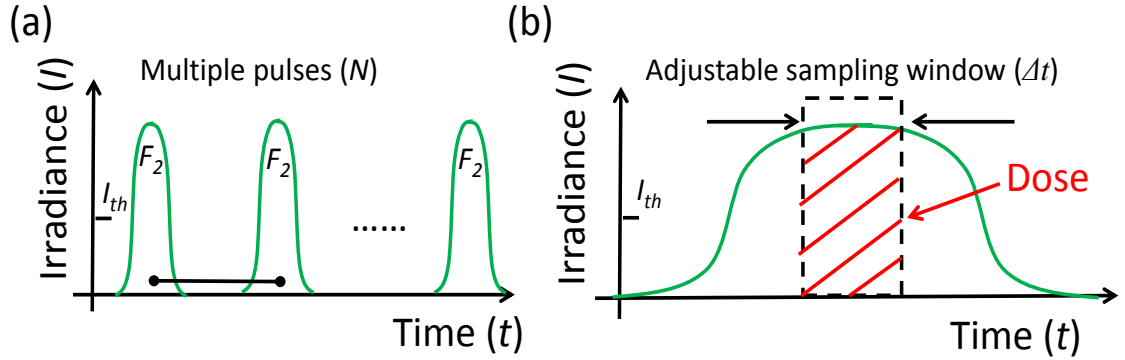
Figure 28: Two different surgical operations are illustrated in (a) and (b), where (a) is the conventional dose control by the counting number (N) of multiple pulses incidence and (b) is the new dose control by sampling a single nanosecond pulse by the ultrafast all-optical shutter with an adjustable sampling window ($\Delta\tau$).

Figure 28(a) exemplifies a conventional surgical operation requiring multiple pulses wherein the fluence per pulse (F) is set by adjusting a variable optical attenuator. F_2 is selected here to ablate the medium for the best volume removal rate. Then, a mechanical shutter lets through a variable number of pulses (N) to achieve the desired ablation volume after a total exposure fluence (dose) $F_{total} = N \cdot F_2$. The ablation diameter and depth after N pulses would be close to N times the ablation diameter and depth for a single pulse. The cut size can be accurately controlled by varying the numbers (N) of incident pulses. Note that to reduce a single cut time using this method one would have to increase the repetition rate of the used laser. However, laser systems with increased repetition rates tend to yield reducing energy per pulse, which results in decreasing fluence values below the damage threshold. Therefore, surgeries are typically conducted using laser with a relatively low repetition rate. For instance, dental surgeries theoretically require repetition rates less than f=380 kHz for a colliding pulse mode-locked dye laser and a dye amplifier (BESTEC, Berlin) with $\tau = 300$ fs, wavelength $\lambda =$

615 nm to preserve a minimum pulse energy of 3 mJ [49]. Otherwise, this laser system was practically operated at a much lower repetition rate for pulsed-laser surgery as $f = 3$ Hz $<<$ 380 kHz to preserve enough energy per pulse. An ablation depth of healthy human dentine with a thickness of 16 μm is achieved after 100 pulses (F=2 Jcm^{-2} per pulse). In this case, a mechanical shutter lets through 100 pulses with a repetition rate of 3 Hz, so the whole single-cut process takes 33 s.

Reducing the overall cutting time in surgeries is nonetheless attractive because it reduces the infection probability and pain of patients. A new dose control system is present here to reduce the single-cut time within the temporal pulse width of a single nanosecond pulse without losing the cut precision and controllability of femtosecond pulsed-laser ablation. The pulsed-laser in this new approach is replaced by a nanosecond laser, potentially reducing the capital equipment costs by avoiding the need of a more expensive femtosecond laser. Figure 28(b) shows that this new dose-control method will be able to sample a slide out of a single nanosecond pulse and ablate tissues by this sampled portion of the laser pulse. This new dose-control enables non-thermal ablations with nanosecond lasers, because the duration of sampled portion of the laser pulse will be reduced down to picosecond to femtosecond region by this method.

In the proposed dose-control method, the total exposure fluence (dose) is now controlled by varying an adjustable sampling window (Δt) and can be written as

$F_{total} = \int_{t_0}^{t_0+\Delta t} I(t)dt$, where t_0 is the beginning time of the sampling window. The proposed

sampling process requires a shutter with an ultrafast temporal response, which mechanical and electrical shutters do not allow. Hence, this research aims to develop an **ultrafast all-optical shutter** which allows implementation of the newly invented dose-control scheme presented in Figure 28(b), and wherein the adjustable sampling window, Δt, can be precisely and easily tuned to meet real-time feedback dose-control requirements for laser surgeries. The **ultrafast all-optical shutter** enables a dramatic

reduction of surgical times and costs by allowing the use of less expensive nanosecond lasers emitting at visible wavelengths.

Let's consider that a signal optical pulse, at 618 nm with a peak irradiance of $I_{in} = 100$ GW/cm^2, entering the input port will be split into two pulses: a first signal optical pulse propagating in a clockwise direction and a second signal optical pulse propagating in a counter-clockwise direction with an equal peak irradiance of 50 GW/cm^2. At the **Narrowband NLO Device** both signal optical pulses will impinge at $\pm 45^o$ causing a reflectance change that is at least half of that caused by the control optical pulse. Simulations of the nonlinear response as shown in CHAPTER 3 of the **Narrowband NLO Device** indicate that the maximum reflectance change self-induced by a signal optical pulse on the **Narrowband NLO Device** is $\Delta R_2 = -17\%$. In contrast, the control pulse is expected to induce a maximum reflectance change of $\Delta R_1 = -47\%$, where the control optical pulse is injected at normal incidence, 570 nm, and with a peak irradiance of 50 GW/cm^2.

In the temporal region of interest wherein the amplitude and phase of the first and second signal pulses are different (Region B shown in Figure 24), the relative phase-shift between the first and second signal optical pulses is $\varnothing_1 - \varnothing_2 = \Delta\varnothing_1 - \Delta\varnothing_2 \sim 0.278$(rad), and their total reflectance are $R_1 = R_0 + \Delta R_1 = 40\%$ and $R_2 = R_0 + \Delta R_2 = 70\%$, where $R_0 = 87\%$ is the linear reflectance. Using the values of I_{in}, R_1, R_2, and $\varnothing_1 - \varnothing_2$ in the interferometric Eq. 4-3, we calculate a peak output irradiance of $I_{out} = 2.1$ GW/cm^2 and a minimum fluence of 1 mJ/cm^2 assuming a 500 fs pulse width at the output port. If we reduce the area of the output optical pulse by a factor of a 1000, (i.e. using a microscope objective with a lens power higher than 33×) the peak irradiance (>1 TW/cm^2) and fluence (>1 J/cm^2) will be larger than the ablation threshold of a variety of metals, dielectrics, and biological materials.

4.4 Conclusion

The optical layout of the **ultrafast all-optical shutter** consists of a ring interferometer and a nonlinear optical device producing strong reflectance changes at visible wavelengths optically excited by a control pulse. The impulse response of the shutter is measured using a temporal-scan experiment. The ultrafast temporal response shows that the shutter opens and closes faster than 1 ps controlled by a femtosecond laser pulse, and the adjustable opening time of the shutter is easily and precisely preset between 3.2 ps to 12 ps with a constant interval of 0.8 ps.

The results in CHAPTER 4 have been prepared in a paper draft. A provisional patent covering the all-optical shutter described in this chapter: "Ultrafast all-optical shutter for medical and laser manufacturing applications," (GTRC ID 6378) has been filed to the Georgia Tech office of Technology Licensing.

CHAPTER 5: CONCLUSIONS AND FUTURE WORK

5.1 Conclusions

Ultrafast optical applications using all-optical controls at visible wavelengths have been limited by the lack of materials and devices with a strong nonlinear optical (NLO) response. Noble metals are known to have extremely large and ultrafast NLO response at visible wavelengths, and their complex refractive index changes ($\Delta N = \Delta n + i\Delta k$) excited all-optically are orders-of-magnitude larger than can be found in other known NLO materials. For instance, a peak value of $\Delta N = 0.39 + i0.1$ at 545 nm has been extracted for a 23 nm-thick Au film pumped by a peak pulse irradiance of 13 GW/cm^2 (total fluence 16 J/m^2) and a pulse width of 60 fs. In the visible spectrum, other known NLO materials show much smaller values of ΔN: at 532 nm polythiophene displays a $\Delta N = 9.9 \times 10^{-5}$ for a peak pulse irradiance of 7 GW/cm^2 (total fluence 2660 J/m^2) and a pulse width of 38 ps [81]; at 576 nm CdS$_x$Se$_{1-x}$ semiconductor-doped glass display a $\Delta N = -3.8 \times 10^{-5}$ at a peak pulse irradiance of 12 GW/cm^2 (total fluence 240 J/m^2) and a pulse width of 2 ps [82]; at 532 nm ZnSe displays a $\Delta N = -1.2 \times 10^{-4}$ for a peak pulse irradiance of 1 GW/cm^2 (total fluence 270 J/m^2) and a pulse width of 27 ps [83]. Note that although a direct comparison is not easily made, regardless of the experimental conditions, the values of ΔN that can be achieved in noble metals such as Au, are significantly larger than the values reported in the literature.

However, the transmittance and reflectance changes provided by a single noble metal thin-film layer are still not strong enough compared to large amplitude and/or phase modulations of optical signals needed in all-optical control applications. In this

work, the research was divided into three parts to understand how the linear and NLO properties of these noble metal thin films can be engineered and optimized to overcome a wide variety of requirements in ultrafast optical applications.

First, the NLO properties of Au and Ag/Au bilayer metallic thin films are described as an ultrafast electron and lattice heating process using comprehensive physical models compared with experiments. This study shows that the linear and NLO properties of bilayer metallic films can both be tuned in the visible spectral region by controlling the mass-thickness ratio between Au and Ag. The combined properties of these bilayers are therefore attractive for different photonic applications illustrated by plasmonic devices and optical filters.

Second, the understanding of NLO response of metallic films leads to the development of NLO devices, which can further amplify the ultrafast thermal nonlinearities of noble metals. The NLO device structure consists of four thin-film layers and can be engineered to display strong reflectance changes with very broad spectral and angular bandwidths across the visible spectral region. Upon being excited by a femtosecond optical pulse, an improved change of reflectance up to 25 times was observed when comparing the NLO device with a single Au film, having the same Au thickness, on a glass substrate. The reflectance change of the NLO device is ultrafast. The linear and NLO properties of these NLO devices can also be engineered to present narrow spectral and angular bandwidths while preserving a strong NLO response. The adjustable bandwidth of NLO device designs transforms all-optical controls not only for low peak-power but also for high peak-power signal pulses applications.

Third, the development of the NLO device technology was integrated into an ultrafast optical system. The temporal-scan experiments show that the ultrafast all-optical shutter opens and closes by an ultrafast temporal response faster than 1 ps excited by a

femtosecond control pulse, and its adjustable opening window was demonstrated to be precisely and easily tunable from 3.2 to 12 ps.

5.2 Future work

This dissertation presents a comprehensive study of the linear and NLO properties of noble metal thin films, and NLO devices that lead to a large enhancement of their ultrafast NLO responses. Research work can be expanded taking the NLO device designs presented in this dissertation, as a starting point, to further amplify the NLO response. Possible approaches include inclusion of nonlinear dielectrics and a cascaded connection of the NLO devices wherein a signal pulse passes multiple times.

Since the metal-dielectric thin-film structures (**Broadband** and **Narrowband NLO Devices**) contain four components layers by two dielectric layers and two noble metal (Au and Ag) layers, it would be interesting to incorporate dielectric layers with strong NLO properties. Therefore, the nonlinearities of the whole structure could be completely exploited and cause further enhancement by nonlinearities not only from the metal layer but also superimposing with nonlinear dielectric layers. Note that the initial structure is designed only to amplify ultrafast thermal nonlinearities of its component Au layer. When superimposing the other NLO properties from dielectric layers, the total enhancement effect should not be decreased. Since the driving force of ultrafast thermal nonlinearities originates from the density of absorbed power, which is proportional to the linear absorptance in a metal layer, the NLO dielectric layer candidate should have a relatively low linear absorptance to preserve the linear absorption properties of the metal layer in order to excite its NLO response.

One possible future research direction is to study NLO dielectrics such as Au or Ag nanoparticles doped dielectric composite films, where their dielectric host are transparent such as SiO_2 and polyvinylpyrrolidone (PVP) [84], which shows large

nonlinear absorptions and nonlinear refractive indices based on the third-order nonlinear susceptibility $\chi^{(3)}$ process.

In addition to the inclusion of NLO dielectrics in the structure, the other approach of accessing a larger NLO response without changing the material composition in NLO devices is to impose a cascade connection on a single NLO device. Figure 29 shows possible geometry for coupling a signal pulse into a glass slab waveguide and form the cascade connection at the **Narrowband NLO Device**. Here, a 1.5 mm-thick glass substrate (Ex: VWR Micro Slides glass) is used as a glass slab waveguide, and the four layer metal-dielectric thin-film structure can be deposited on top of this glass substrate with a patterned length of 6 mm by an e-beam deposition system with a shadow mask. Prism 1 and 2 are two right-angle prisms for coupling the signal pulse in and out the glass slab waveguide. The signal pulse can be coupled into the slab waveguide at the incidence angle of 45˚, which matches the total reflection angle at the interface between air and glass. After a signal pulse is coupled into the glass slab waveguide, it would reflect off the **Narrowband NLO Device** twice, and experience two nonlinear reflection coefficient changes excited by the same control pulse. The result of doubling NLO interactions between a signal pulse and the **Narrowband NLO Device** cascades two amplitude and/or phase modulations. The total cascaded signal modulations is expected to be increased compared to a single non-cascaded modulation in a simulation study. The future research work can therefore be directed to optimize the cascaded signal modulations by multiple

optical passes through the **Narrowband NLO Device**.

Narrowband NLO Device
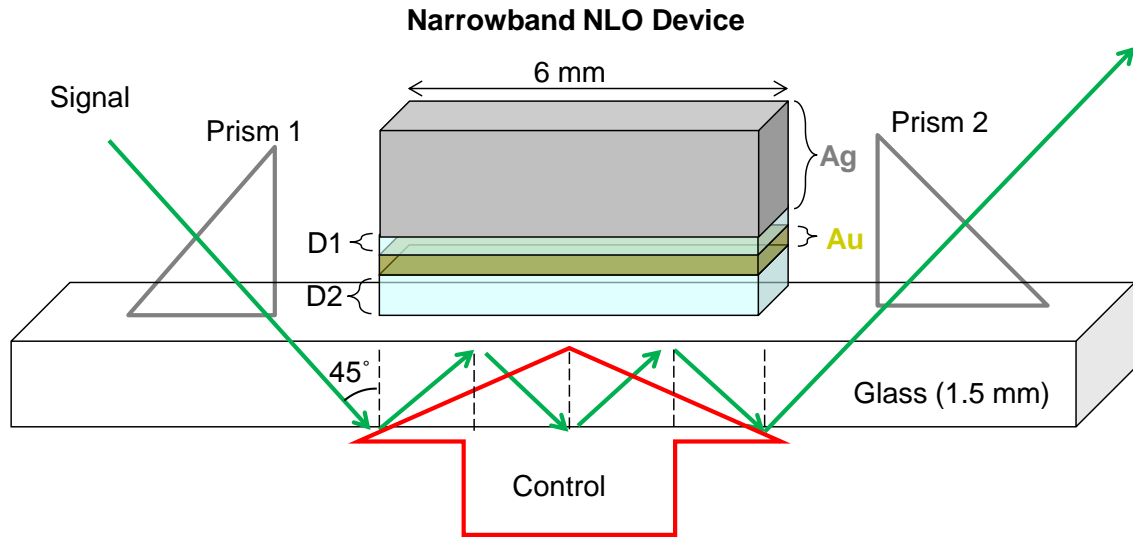
Figure 29: Cascaded beam geometry imposed on the Narrowband NLO Device by a glass slab waveguide, where a signal pulse enters the waveguide at the incidence angle of 45°, double passes through the device in a reflection mode, and overlaps temporally and spatially with a control pulse coming at the normal incidence; Prism 1 and 2 are two right-angle prisms for coupling in and out the signal pulse.

Although the continuous study in amplifying the NLO properties of metal-dielectric thin-film structures is always attractive for ultrafast optical applications, it is also worthwhile to understand ultrafast optical applications that could benefit from the all-optical control technology presented in this dissertation.

A wide variety of possible optical applications were discovered through a National Science Foundation (NSF-iCORPS) program through many interviews with people in the related industry and academic field. Lessons learned from NSF-iCORPS program helped to identify potential avenues of future research and their potential for commercialization.

The **ultrafast all-optical shutter** was first conceived as a novel way to extract a high peak-power sub-nanosecond laser pulse out of a nanosecond laser pulse. The potential impact of such an approach is that it could enable a low-cost, high speed, and easily maintenance sub-nanosecond laser to provide high resolution non-thermal ablation. Future work towards development of a high peak-power sub-nanosecond laser pulse

79

extraction system will require integrating the **ultrafast all-optical shutter** into a single nanosecond laser. A major challenge for this will be to sharpen the fast rising edge of a control optical pulse from a nanosecond seed pulse. The possible solution is to generate a sharp rising edge optical pulse by passing a nanosecond pulse through a slow saturable absorber, for example, an organic dye DODCI (3, 3'- diethyloxadicarbocyanine iodide) [80]. Because the sub-nanosecond pulse extracted by the **ultrafast all-optical shutter** is expected to create a unique temporal pulse shape (flat-hat like) as shown in Figure 28(b), it will be interested to study if materials could therefore be non-thermally ablated resulting in a high cutting resolution.

On the other hand, other potential applications, discovered through NSF-iCORPS program are first to use the **ultrafast all-optical shutter** as a temporal pulse shaping device (from the discussion with Dr. Brian D. Sheehy and Dr. Trivene Rao from Brookhaven National Laboratory). The temporally shaped optical pulse could be converted into a short electron pulse by passing through a photocathode based on the photon-electric effect. The high photoelectrons generation efficiency and an adjustable temporal pulse width within tens of picoseconds could be enabled. Then, the short X-ray pulse is able to be emitted by passing electron pulses through the X-ray tube. Both short electron pulses and X-ray pulses are powerful laboratory tools in fundamental studies, and X-ray pulses also have potential impacts in medical imaging applications.

The second path is to use the **ultrafast all-optical shutter** as an ultrafast camera for ultrafast photography. Although ultrafast events such as visualizing light propagation can be captured by a streak camera, each image frame needs to be scanned and reconstructed through a multiple of captured lines [85]. The ultrafast camera will be interested to develop with a single shot per imaging frame ability with the **ultrafast all-optical shutter** to improve the image quality and recording speed.

The final path is to use the **ultrafast all-optical shutter** as a biomedical imaging device for seeing through scattering medium, for example, imaging blood vessels beneath

skins. It is inspired by the discussion with vascular surgeons such as Prof. Yazan Duwari, and related imaging research teams in optical coherence tomography (OCT) and diffuse optical tomography (DOT). The initial concept is to adopt **ultrafast all-optical shutter** to demonstrate ballistic-photon imaging using a time-gated optical image technique studied in our research group in the past [86].

5.3 Publications

Journal Articles

1. J. Hsu, C. Fuentes-Hernandez, A. R. Ernst, J. M. Hales, J. W. Perry, and B. Kippelen, "*Linear and nonlinear optical properties of Ag/Au bilayer thin films,*" Optics Express 20, 8629-8864 (2012).

2. J. Hsu, C. Fuentes-Hernandez, A. R. Ernst, and B. Kippelen, "*Ultrafast nonlinear mirrors with broad spectral and angular bandwidths in the visible spectral range,*" Optics Express 21, 3575-3581 (2013).

3. J. Hsu, C. Fuentes-Hernandez, J. M. Hales, J. W. Perry, and B. Kippelen, "*Angular sensitivity of nonlinear optical dual metal-layer device for all-optical control of high intensity signal pulse,*" prepared for publication in Optics Letter.

4. J. Hsu, C. Fuentes-Hernandez, J. M. Hales, J. W. Perry, and B. Kippelen, "*Ultrafast all-optical shutter at visible wavelengths,*" prepared for publication.

5. Y. H. Zhou, C. Fuentes-Hernandez, T. M. Khan, J. C. Liu, J. Hsu, J. W. Shim, A. Dindar, J. P. Youngblood, R. J. Moon, and B. Kippelen, "*Recyclable organic solar cells on cellulose nanocrystal substrates,*" Scientific Reports **3**, 1536 (2013).

Provisional patents

1. J. Hsu, C. Fuentes-Hernandez, A. R. Ernst, and B. Kippelen, "*Nonlinear optical devices for ultrafast optical applications,*" (GTRC 6221) filed to the Georgia Tech office of Technology Licensing.

2. J. Hsu, C. Fuentes-Hernandez, and B. Kippelen, "*Ultrafast all-optical shutter for medical and laser manufacturing applications,*" (GTRC 6378) filed to the Georgia Tech office of Technology Licensing.

Conferences

1. J. Hsu, D. T. Owens, C. Fuentes-Hernandez, and B. Kippelen, "*Metamaterial metal-dielectric photonic bandgap filters with high inband transmittance and strong out-of-band rejection,*" in Tri-Service Metamaterial Review (Virginia Beach, VA, USA, 2010).

2. C. Fuentes-Hernandez, D. Owens, J. Hsu, A. R. Ernst, J. M. Hales, J. W. Perry, and B. Kippelen, "*The nonlinear optical response of transparent silver/gold multi-metal layers,*" in *Active Photonic Materials III*, Proceedings of SPIE (SPIE, San Diego, CA, USA, 2010), 7756, pp. 77560G.

3. C. Fuentes-Hernandez, J. Hsu, D. T. Owens, A. R. Ernst, J. M. Hales, J. W. Perry, and B. Kippelen, "Amplification of the nonlinear optical response of metals in induced transmission filters," in *Active photonic Materials IV* (SPIE, San Diego, CA,USA, 2011), pp. 8095-11.

4. J. Hsu, A. R. Ernst, D. T. Owens, C. Fuentes-Hernandez, J. M. Hales, J. W. Perry, and B. Kippelen, "*The nonlinear optical response of metals and metal-dielectric transparent multi-layers,*" in *COPE OPEN HOUSE* (Georgia Institute of Technology, Atlanta, GA, USA, 2011).

5. J. Hsu, C. Fuentes-Hernandez, A. R. Ernst, and B. Kippelen, "*Noble metal nonlinear optical mirrors,*" in *Southeast Ultrafast Conference* (SEUFC, Atlanta, GA, USA, 2013).

6. J. Hsu, C. Fuentes-Hernandez, A. R. Ernst, and B. Kippelen, "*Noble metal nonlinear optical mirrors with adjustable spectral and angular bandwidths for all-optical controls at visible wavelengths,*" in *Advanced NLO Concepts* (CLEO, San Jose, CA,USA, 2013), p. CTu3E.8.

7. J. Hsu, C. Fuentes-Hernandez, A. R. Ernst, and B. Kippelen, "*Ultrafast nonlinear optical mirrors for all-optical applications at visible wavelengths,*" in *Novel Non-Linear Photonic Platforms* (SPIE, San Diego, CA,USA, 2013), pp. 8808-48.

REFERENCES

1.   W. L. Barnes, A. Dereux, and T. W. Ebbesen, "Surface plasmon subwavelength optics," Nature **424**, 824-830 (2003).

2.   H. T. Chen, W. J. Padilla, J. M. O. Zide, A. C. Gossard, A. J. Taylor, and R. D. Averitt, "Active terahertz metamaterial devices," Nature **444**, 597-600 (2006).

3.   D. T. Owens, C. Fuentes-Hernandez, J. M. Hales, J. W. Perry, and B. Kippelen, "Nonlinear optical properties of induced transmission filters," Opt. Express **18**, 19101-19113 (2010).

4.   M. J. Bloemer and M. Scalora, "Transmissive properties of Ag/MgF2 photonic band gaps," Appl. Phys. Lett. **72**, 1676-1678 (1998).

5.   S. Y. Ryu, C. H. Lee, I. S. Oh, S. Y. Song, K. H. Hwang, H. S. Hwang, M. H. Han, B. H. Hwang, H. K. Baik, Y. S. Kim, and J. Y. Lee, "Efficient inverted top-emitting organic light emitting diodes with transparent and surface-modified multilayer anodes," Electrochem. Solid State Lett. **13**, J43-J46 (2010).

6.   N. Rotenberg, A. D. Bristow, M. Pfeiffer, M. Betz, and H. M. van Driel, "Nonlinear absorption in Au films: Role of thermal effects," Phys. Rev. B **75**, 155426 (2007).

7.   D. T. Owens, C. Fuentes-Hernandez, J. M. Hales, J. W. Perry, and B. Kippelen, "A comprehensive analysis of the contributions to the nonlinear optical properties of thin Ag films," J. Appl. Phys. **107**, 123114 (2010).

8.   M. A. Swillam, N. Rotenberg, and H. M. van Driel, "All-optical ultrafast control of beaming through a single sub-wavelength aperture in a metal film," Opt. Express **19**, 7856-7864 (2011).

9.   G. A. Wurtz, PollardR, HendrenW, G. P. Wiederrecht, D. J. Gosztola, V. A. Podolskiy, and A. V. Zayats, "Designed ultrafast optical nonlinearity in a plasmonic nanorod metamaterial enhanced by nonlocality," Nature Nanotechnology **6**, 107-111 (2011).

10. N. Rotenberg, M. Betz, and H. M. van Driel, "Ultrafast all-optical coupling of light to surface plasmon polaritons on plain metal surfaces," Phys. Rev. Lett. **105**, 017402 (2010).

11. J. Y. Zhang, L. Wang, S. Krishna, M. Sheik-Bahae, and S. R. J. Brueck, "Saturation of the second harmonic generation from GaAs-filled metallic hole arrays by nonlinear absorption," Phys. Rev. B **83**, 165438 (2011).

12. S. I. Anisimov, B. L. Kapeliovich, and T. L. Perel'Man, "Electron emission from metal surfaces exposed to ultrashort laser pulses," Sov. Phys. JETP **39**, 375-377 (1974).

13. M. Sheik-Bahae, A. A. Said, T. H. Wei, D. J. Hagan, and E. W. Vanstryland, "Sensitive measurement of optical nonlinearities using a single beam," IEEE Journal of Quantum Electronics **26**, 760-769 (1990).

14. G. Yang, D. Y. Guan, W. T. Wang, W. D. Wu, and Z. H. Chen, "The inherent optical nonlinearities of thin silver films," Optical Materials **25**, 439-443 (2004).

15. D. Ricard, P. Roussignol, and C. Flytzanis, "Surface-mediated enhancement of optical-phase conjugation in metal colloids," Optics Letters **10**, 511-513 (1985).

16. N. N. Lepeshkin, W. Kim, V. P. Safonov, J. G. Zhu, R. L. Armstrong, C. W. White, R. A. Zuhr, and V. M. Shalaev, "Optical nonlinearities of metal-dielectric composites," Journal of Nonlinear Optical Physics & Materials **8**, 191-210 (1999).

17. K. Uchida, S. Kaneko, S. Omi, C. Hata, H. Tanji, Y. Asahara, A. J. Ikushima, T. Tokizaki, and A. Nakamura, "Optical nonlinearities of a high concentration of small metal particles dispersed in glass - copper and silver particles," Journal of the Optical Society of America B **11**, 1236-1243 (1994).

18. C. K. Sun, F. Vallee, L. H. Acioli, E. P. Ippen, and J. G. Fujimoto, "Femtosecond-tunable measurement of electron thermalization in gold," Phys. Rev. B **50**, 15337-15348 (1994).

19. H. E. Elsayedali, T. B. Norris, M. A. Pessot, and G. A. Mourou, "Time-resolved observation of electron-phonon relaxation in copper," Phys. Rev. Lett. **58**, 1212-1215 (1987).

20. H. Baida, D. Mongin, D. Christofilos, G. Bachelier, A. Crut, P. Maioli, N. Del Fatti, and F. Vallee, "Ultrafast nonlinear optical response of a single gold nanorod near its surface plasmon resonance," Phys. Rev. Lett. **107**, 057402 (2011).

21. O. L. Muskens, N. Del Fatti, and F. Vallee, "Femtosecond response of a single metal nanoparticle," Nano Letters **6**, 552-556 (2006).

22. R. Rosei and D. W. Lynch, "Thermomodulation spectra of Al, Au, and Cu," Phys. Rev. B **5**, 3883-3894 (1972).

23. R. Rosei, C. H. Culp, and J. H. Weaver, "Temperature modulation of optical-transitions involving Fermi-surface in Ag : Experimental," Phys. Rev. B **10**, 484-489 (1974).

24. G. L. Eesley, "Observation of non-equilibrium electron heating in copper," Phys. Rev. Lett. **51**, 2140-2143 (1983).

25. J. Hohlfeld, S. S. Wellershoff, J. Gudde, U. Conrad, V. Jahnke, and E. Matthias, "Electron and lattice dynamics following optical excitation of metals," Chemical Physics **251**, 237-258 (2000).

26. C. Voisin, N. Del Fatti, D. Christofilos, and F. Vallee, "Ultrafast electron dynamics and optical nonlinearities in metal nanoparticles," J. Phys. Chem. B **105**, 2264-2280 (2001).

27. M. Conforti and G. Della Valle, "Derivation of third-order nonlinear susceptibility of thin metal films as a delayed optical response," Phys. Rev. B **85**, 245423 (2012).

28. R. W. Boyd, *Nonlinear Optics,* Third ed. (Academic Press, Inc. , 2008), pp. 212-213.

29. B. Buchalter and G. R. Meredith, "Third-order optical susceptibility of glasses determined by third harmonic generation," Appl. Opt. **21**, 3221-3224 (1982).

30. J. E. Ehrlich, J. D. Valera, H. Adachihara, J. V. Moloney, and A. C. Walker, "Nonlinear refraction and absorption in 4BCMU planar waveguides at 1.064 μm wavelength," Journal of Modern Optics **40**, 2151-2160 (1993).

31.   J. M. Hales, S. J. Zheng, S. Barlow, S. R. Marder, and J. W. Perry, "Bisdioxaborine polymethines with large third-order nonlinearities for all-optical signal processing," Journal of the American Chemical Society **128**, 11362-11363 (2006).

32.   H. Nasu and J. D. Mackenzie, "Nonlinear optical-properties of glasses and glass-based or gel-based composites," Optical Engineering **26**, 102-106 (1987).

33.   H. B. Liao, R. F. Xiao, J. S. Fu, H. Wang, K. S. Wong, and G. K. L. Wong, "Origin of third-order optical nonlinearity in Au : SiO2 composite films on femtosecond and picosecond time scales," Optics Letters **23**, 388-390 (1998).

34.   B. L. Lawrence, M. Cha, J. U. Kang, W. Toruellas, G. Stegeman, G. Baker, J. Meth, and S. Etemad, "Large purely refractive nonlinear index of single crystal P-toluene sulphonate (PTS) at 1600 nm," Electronics Letters **30**, 447-448 (1994).

35.   P. E. Hopkins, "Influence of Inter- and Intraband Transitions to Electron Temperature Decay in Noble Metals After Short-Pulsed Laser Heating," J. Heat Transf.-Trans. ASME **132**, 122402 (2010).

36.   G. D'Aguanno, N. Mattiucci, M. J. Bloemer, and M. Scalora, "Accessing quadratic nonlinearities of metals through metallodielectric photonic-band-gap structures," Phys. Rev. E **74**, 036605 (2006).

37.   W. J. Scouler, "Temperature-modulated reflectance of gold from 2 to 10 ev," Phys. Rev. Lett. **18**, 445-448 (1967).

38.   L. Brzozowski and E. H. Sargent, "Optical signal processing using nonlinear distributed feedback structures," IEEE Journal of Quantum Electronics **36**, 550-555 (2000).

39.   Y. B. Band, D. J. Harter, and R. Bavli, "Optical pulse compressor composed of saturable and reverse saturable absorbers," Chem. Phys. Lett. **126**, 280-284 (1986).

40.   D. J. Harter, M. L. Shand, and Y. B. Band, "Power energy limiter using reverse saturable absorption," J. Appl. Phys. **56**, 865-868 (1984).

41. C. S. Yelleswarapu, S. R. Kothapalli, and D. Rao, "Optical Fourier techniques for medical image processing and phase contrast imaging," Opt. Commun. **281**, 1876-1888 (2008).

42. C. S. Yelleswarapu, P. F. Wu, S. R. Kothapalli, D. Rao, B. R. Kimball, S. S. S. Sai, R. Gowrishankar, and S. Sivaramakrishnan, "All-optical spatial filtering with power limiting materials," Opt. Express **14**, 1451-1457 (2006).

43. K. A. Stankov, "A mirror with an intensity-dependent reflection coefficient," Appl. Phys. B **45**, 191-195 (1988).

44. J. B. Dherbecourt, A. Denoeud, J. M. Melkonian, M. Raybaut, A. Godard, M. Lefebvre, and E. Rosencher, "Picosecond tunable mode locking of a Cr(2+):ZnSe laser with a nonlinear mirror," Optics Letters **36**, 751-753 (2011).

45. L. Brzozowski, V. Sukhovatkin, E. T. H. Sargent, A. T. J. SpringThorpe, and M. Extavour, "Intensity-dependent reflectance and transmittance of semiconductor periodic structures," IEEE J. Quantum Electron. **39**, 924-930 (2003).

46. M. Sheik-Bahae, D. J. Hagan, and E. W. Vanstryland, "Dispersion and band-gap scaling of the electronic Kerr effect in solids associated with two-photon absorption," Phys. Rev. Lett. **65**, 96-99 (1990).

47. S. H. Chung and E. Mazur, "Surgical applications of femtosecond lasers," J. Biophotonics **2**, 557-572 (2009).

48. R. Birngruber, C. A. Puliafito, A. Gawande, W. Z. Lin, R. W. Schoenlein, and J. G. Fujimoto, "Femtosecond laser tissue interactions - retinal injury studies," IEEE Journal of Quantum Electronics **23**, 1836-1844 (1987).

49. J. Kruger, W. Kautek, and H. Newesely, "Femtosecond-pulse laser ablation of dental hydroxyapatite and single-crystalline fluoroapatite," Appl. Phys. A **69**, S403-S407 (1999).

50. N. Nishimura, C. B. Schaffer, B. Friedman, P. S. Tsai, P. D. Lyden, and D. Kleinfeld, "Targeted insult to subsurface cortical blood vessels using ultrashort laser pulses: three models of stroke," Nat. Methods **3**, 99-108 (2006).

51. C. L. Hoy, W. N. Everett, M. Yildirim, J. Kobler, S. M. Zeitels, and A. Ben-Yakar, "Towards endoscopic ultrafast laser microsurgery of vocal folds," J. Biomed. Opt. **17**, 038002 (2012).

52. A. A. Oraevsky, L. B. DaSilva, A. M. Rubenchik, M. D. Feit, M. E. Glinsky, M. D. Perry, B. M. Mammini, W. Small, and B. C. Stuart, "Plasma mediated ablation of biological tissues with nanosecond-to-femtosecond laser pulses: Relative role of linear and nonlinear absorption," IEEE J. Sel. Top. Quantum Electron. **2**, 801-809 (1996).

53. J. Cheng, C. S. Liu, S. Shang, D. Liu, W. Perrie, G. Dearden, and K. Watkins, "A review of ultrafast laser materials micromachining," Opt. Laser Technol. **46**, 88-102 (2013).

54. B. H. Ong, X. C. Yuan, and S. C. Tjin, "Bimetallic silver-gold film waveguide surface plasmon resonance sensor," Fiber Integrated Opt. **26**, 229-240 (2007).

55. H. Tohati, A. Sipos, G. Szekeres, A. Mathesz, A. Szalai, P. Jojart, J. Budai, C. Vass, A. Kohazi-Kis, M. Csete, and Z. Bor, "Surface plasmon scattering on polymer-bimetal layer covered fused silica gratings generated by laser induced backside wet etching," Appl. Surf. Sci. **255**, 5130-5137 (2009).

56. M. Thomschke, S. Hofmann, S. Olthof, M. Anderson, H. Kleemann, M. Schober, B. Lussem, and K. Leo, "Improvement of voltage and charge balance in inverted top-emitting organic electroluminescent diodes comprising doped transport layers by thermal annealing," Appl. Phys. Lett. **98**, 083304 (2011).

57. T. Q. Qiu, T. Juhasz, C. Suarez, W. E. Bron, and C. L. Tien, "Femtosecond laser-heating of multilayer metals .2. Experiments," Int. J. Heat Mass Transf. **37**, 2799-2808 (1994).

58. T. Q. Qiu and C. L. Tien, "Femtosecond laser-heating of multilayer metals .1. Analysis," Int. J. Heat Mass Transf. **37**, 2789-2797 (1994).

59. M. G. Blaber, M. D. Arnold, and M. J. Ford, "A review of the optical properties of alloys and intermetallics for plasmonics," J. Phys.-Condes. Matter **22**, 143201 (2010).

60. H. A. Macleod, "The induced-transmission filter," in *Thin-Film Optical Filters,* Third ed. (Institude of Physics Publishing, London, 2001).

61. Z. Lin, L. V. Zhigilei, and V. Celli, "Electron-phonon coupling and electron heat capacity of metals under conditions of strong electron-phonon nonequilibrium," Phys. Rev. B **77**, 075133 (2008).

62. J. Y. Bigot, J. Y. Merle, O. Cregut, and A. Daunois, "Electron dynamics in copper metallic nanoparticles probed with femtosecond optical pulses," Phys. Rev. Lett. **75**, 4702-4705 (1995).

63. P. G. Etchegoin, E. C. Le Ru, and M. Meyer, "An analytic model for the optical properties of gold," J. Chem. Phys. **125**, 164705 (2006).

64. J. Hsu, C. Fuentes-Hernandez, A. R. Ernst, J. M. Hales, J. W. Perry, and B. Kippelen, "Linear and nonlinear optical properties of Ag/Au bilayer thin films," Opt. Express **20**, 8629-8864 (2012).

65. R. W. Schoenlein, W. Z. Lin, J. G. Fujimoto, and G. L. Eesley, "Femtosecond studies of nonequilibrium electronic processes in metals," Phys. Rev. Lett. **58**, 1680-1683 (1987).

66. O. Wada, "Femtosecond all-optical devices for ultrafast communication and signal processing," New J. Phys. **6**, 183 (2004).

67. C. Koos, P. Vorreau, T. Vallaitis, P. Dumon, W. Bogaerts, R. Baets, B. Esembeson, I. Biaggio, T. Michinobu, F. Diederich, W. Freude, and J. Leuthold, "All-optical high-speed signal processing with silicon-organic hybrid slot waveguidesx," Nat. Photonics **3**, 216-219 (2009).

68. I. Ogura, Y. Hashimoto, H. Kurita, T. Shimizu, and H. Yokoyama, "Picosecond all-optical gate using a saturable absorber in mode-locked laser diodes," IEEE Photonics Technol. Lett. **10**, 603-605 (1998).

69. A. M. C. Dawes, L. Illing, S. M. Clark, and D. J. Gauthier, "All-optical switching in rubidium vapor," Science **308**, 672-674 (2005).

70. D. A. Braje, V. Balić, G. Y. Yin, and S. E. Harris, "Low-light-level nonlinear optics with slow light," Phys. Rev. A **68**, 041801 (2003).

71. M. A. Duguay and J. W. Hansen, "An ultrafast light gate," Appl. Phys. Lett. **15**, 192 (1969).

72. M. A. M. Versteegh and J. I. Dijkhuis, "Ultrafast all-optical shutter based on two-photon absorption," Optics Letters **36**, 2776-2778 (2011).

73. B. L. Yu, A. B. Bykov, T. Qiu, P. P. Ho, R. R. Alfano, and N. Borrelli, "Femtosecond optical Kerr shutter using lead-bismuth-gallium oxide glass," Opt. Commun. **215**, 407-411 (2003).

74. D. Owen, "Linear and nonlinear optical properties of metal-dielectric multilayer structures," Dissertation (Georgia Institute of Technology, Atlanta, 2010).

75. P. Toliver, R. J. Runser, I. Glesk, and P. R. Prucnal, "Comparison of three nonlinear interferometric optical switch geometries," Opt. Commun. **175**, 365-373 (2000).

76. J. P. Sokoloff, P. R. Prucnal, I. Glesk, and M. Kane, "A terahertz optical asymmetric demultiplexer (TOAD)," IEEE Photonics Technol. Lett. **5**, 787-790 (1993).

77. K. T. McDonald and L. J. Wang, "Bunching of photons when two beams pass through a beam splitter," in *arXiv* (Cornell University Library 2003), pp. arXiv:quant-ph/0312032.

78. V. Degiorgio, "Phase-shift between the transmitted and the reflected optical-fields of a semi-reflecting lossless mirror is pi-2," Am. J. Phys. **48**, 81-82 (1980).

79. D. B. Mortimore, "Fiber loop reflectors," J. Lightwave Technol. **6**, 1217-1224 (1988).

80. M. Wittmann and A. Penzkofer, "Saturable absorption dynamics of mode-locking dye DODCI," Appl. Phys. B **65**, 761-769 (1997).

81. X. Q. Zhang, C. S. Wang, G. Y. Lu, and T. C. He, "Third-order nonlinear optical properties of a series of polythiophenes," Chinese Physics Letters **27**, 074201 (2010).

82. W. C. Banyai, N. Finlayson, C. T. Seaton, G. I. Stegeman, M. Oneill, T. J. Cullen, and C. N. Ironside, "Saturation of the nonlinear refractive-index change in a semiconductor-doped glass channel waveguide," Appl. Phys. Lett. **54**, 481-483 (1989).

83. A. A. Said, M. Sheikbahae, D. J. Hagan, T. H. Wei, J. Wang, J. Young, and E. W. Vanstryland, "Determination of bound-electronic and free-carrier nonlinearities in ZnSe, GaAs, CdTe, and ZnTe," Journal of the Optical Society of America B **9**, 405-414 (1992).

84. T. C. He, C. S. Wang, X. Pan, and Y. L. Wang, "Nonlinear optical response of Au and Ag nanoparticles doped polyvinylpyrrolidone thin films," Physics Letters A **373**, 592-595 (2009).

85. A. Velten, D. Wu, A. Jarabo, B. Masia, C. Barsi, C. Joshi, E. Lawson, M. Bawendi, D. Gutierrez, and R. Raskar, "Femto-photography: capturing and visualizing the propagation of light," ACM Transactions on Graphics **32**, 44 (2013).

86. C. Fuentes-Hernandez, G. Ramos-Ortiz, S. Y. Tseng, M. P. Gaj, and B. Kippelen, "Third-harmonic generation and its applications in optical image processing," Journal of Materials Chemistry **19**, 7394-7401 (2009).